SAND REPORT
SAND #2002-8568
Unlimited Release
Printed November 2002

Mechanisms of Dislocation-Grain Boundary Interaction

D. L. Medlin, G. Lucadamo, D. Cohen, K. Gross, S. M. Foiles, J. E. Houston
C. B. Carter, R. C. Pond

Prepared by
Sandia National Laboratories
Albuquerque, New Mexico 87185 and Livermore, California 94550

Sandia is a multiprogram laboratory operated by Sandia Corporation, a Lockheed Martin Company, for the United States Department of Energy under Contract DE-AC04-94AL85000.

Sandia National Laboratories

Issued by Sandia National Laboratories, operated for the United States Department of Energy by Sandia Corporation.

Available to DOE and DOE contractors from
U.S. Department of Energy
Office of Scientific and Technical Information
P.O. Box 62
Oak Ridge, TN 37831

Telephone: (865)576-8401
Facsimile: (865)576-5728
E-Mail: reports@adonis.osti.gov
Online ordering: http://www.doe.gov/bridge

Available to the public from
U.S. Department of Commerce
National Technical Information Service
5285 Port Royal Rd
Springfield, VA 22161

Telephone: (800)553-6847
Facsimile: (703)605-6900
E-Mail: orders@ntis.fedworld.gov
Online order: http://www.ntis.gov/ordering.htm

SAND #2002-8568
Unlimited Release
Printed November 2002

Mechanisms of Dislocation-Grain Boundary Interaction

D.L. Medlin, G. Lucadamo, D. Cohen, K. Gross
Sandia National Laboratories
Livermore, CA 94551

S.M. Foiles, J.E. Houston
Sandia National Laboratories
Albuquerque NM 87123

C.B. Carter
University of Minnesota
Department of Chemical Engineering and Materials Science
Minneapolis, MN 55455

R.C. Pond
Department of Engineering (Materials),
University of Liverpool, Liverpool L69 3BX,
United Kingdom.

Abstract

We present the final report for a Laboratory Directed Research and Development project entitled "Mechanisms of Dislocation-Grain Boundary Interaction." In this project we have investigated the fundamental connections between dislocations and grain boundaries. A new dislocation-based model for high angle grain boundary structure has been developed. This work shows that Shockley Partial Dislocations are an important structural element of grain boundaries. We apply this approach to showing how the structure of dissociated, three-dimensional boundaries is directly connected to intergranular misorientation. We have also established how grain boundary steps possessing dislocation content (disconnections) can accommodate interfacial coherency strains. This is an important step towards determining the connection between boundary inclination and localization of interfacial strain. Finally, we have investigated the evolution of grain boundary morphology and its connection to dislocation interactions. This work has identified a mechanism for dislocation emission at grain boundary junctions.

This page intentionally left blank.

Contents

(This page intentionally left blank)

1. Introduction

Incorporating the localized atomistic and microscopic effects of internal interfaces on materials properties and long-term behavior is a significant challenge for large-scale materials simulations. Critical to improving such models is developing an improved understanding of the dislocation-grain boundary interactions that ultimately control the interfacial response to strain. Such interactions impact many materials phenomena and properties including slip transmission, boundary migration, recrystallization, and yield strength and are a critical element in linking atomic structure to continuum behavior. In this report we describe the results of an LDRD project to investigate the behavior of dislocations at grain boundaries. Key accomplishments include the following.

(1) The development of a new, dislocation-based model for grain boundary structure.

In considering the dislocation structures of grain boundaries, it is common to distinguish between low and high angle boundary misorientations. The angular dependence of structure and behavior for low angle boundaries, with misorientations less than 5-10°, is very well modeled by arrays of discrete perfect lattice dislocations. It is difficult, however, to extend such a description to higher angles because the cores of the dislocations overlap, and so the appropriate dislocation-based description high angle boundaries has been unclear. Our work shows that high angle boundaries can be described in terms of arrays of *Shockley partial dislocations* (rather than perfect lattice dislocations). We develop this idea in Chapter 2 and show how it is of utility in predicting the structures of dissociated, 3-dimensional boundaries in Chapter 3.

(2) Determination of how grain boundary steps accommodate coherency strains

In Chapter 4, we analyze the dislocation content of grain boundary steps ("disconnections") to determine how interfacial coherency strains are accommodated by these defects. This work shows the important coupling between boundary inclination (which determines the step density) and the local structure and strain distribution.

(3) Mechanism for dislocation emission at grain boundary junctions

We performed several *in situ* TEM studies to investigate the evolution of grain boundary morphology and its connection to dislocation interactions. This work is described in Chapter 5, which focusses on the morphological evolution of facetted boundaries, and Chapter 6, which investigates the behavior of dislocations at these boundaries. Our analysis shows how repulsive elastic interaction stresses are sufficient to drive grain boundary dislocations across boundary junctions.

2. Shockley Partial Dislocation Model for Grain Boundary Structure

Shockley partial dislocations (Heidenreich and Shockley, 1948) are well understood in relation to bulk FCC defects: translation of a single Shockley partial on an FCC {111} plane creates a stacking fault, whereas translation of a Shockley partial on every adjacent parallel {111} plane reverses the stacking sequence, twinning the crystal. As we will discuss below, Shockley partial dislocations are also an important structural element of grain boundaries in FCC metals. In this chapter, we show how the misorientation between two FCC crystals may be represented by arrays of Shockley partial dislocations. This geometrical model will form the basic framework for our discussion of grain boundary dissociation in Chapter 3.

2.1 Grain Misorientation in terms of Shockley Partial Dislocations.

Our approach is to determine the distribution of Shockley partial dislocations that would be necessary to account for the *total* orientation change across the boundary. Importantly, the single-crystal, rather than a CSL orientation, serves as the reference orientation. As shown schematically in Figure 2-1, we envision the boundary that would form if an array of Shockley partial dislocations (lying on parallel {111} slip planes with one dislocation on each adjacent {111} plane) were to enter an FCC crystal and glide midway through the crystal before stopping at a plane, {hkl}. This operation transforms a periodic vector, $\mathbf{v_A}$, to the vector $\mathbf{v_B}$ in the reoriented crystal through the following two processes: (1) the reorientation due to the twinning operation of the Shockleys and (2) the shape change produced by the *net* Burgers vector of the dislocation array. This is not to say that a boundary forms by the accumulation of isolated Shockley partial dislocations, but rather to provide a conceptual tool for partitioning the orientation difference across the interface into a specific set of Shockley partial dislocations that are intrinsic to the boundary. However, as we will discuss, these dislocations do have physical significance as structural elements of the boundary.

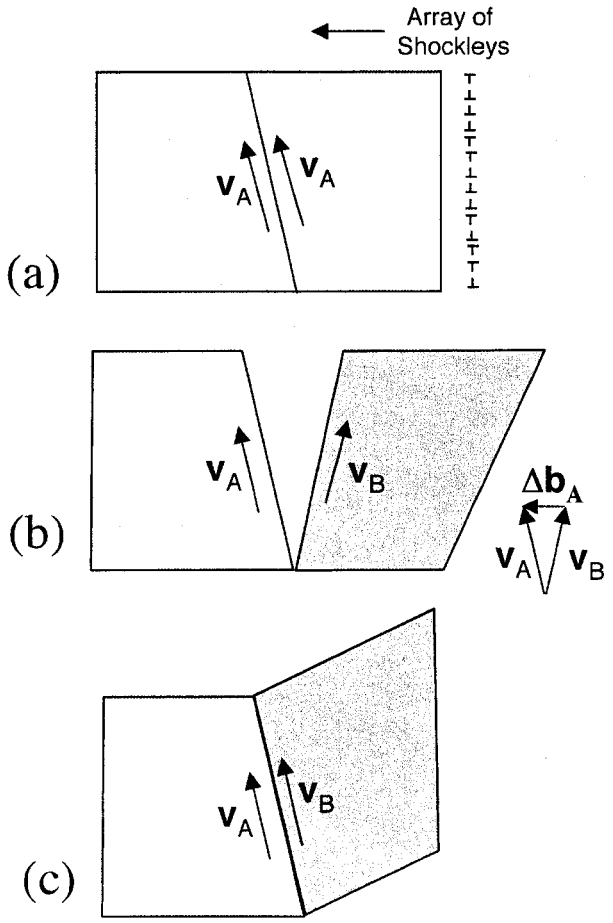

Figure 2-1. Schematic illustrating the orientation changes produced by an array of Shockley partial dislocations. (a) Initial configuration of single crystal A prior to introducing the dislocation array. The interfacial period vector, $\mathbf{v_A}$, is aligned along the plane that will be parallel to the interface in the final bicrystal. The {111} slip planes are horizontal. (b) The array of Shockley partial dislocations has glided into the crystal from the right, stopping at the interface plane identified in (a) to produce a twinning reorientation (a 70.53° rotation), which transforms $\mathbf{v_A}$ to $\mathbf{v_B}$, and a shape change (due to the non-zero Δb_A) in the right side of the crystal (B). Note that $\mathbf{v_B}$ is expressed in the coordinate system of the crystal B. (c) The twinned crystal B, is rotated to fill in the gap produced by the shape change, making $\mathbf{v_A}$ parallel to $\mathbf{v_B}$.

We focus here on <110> tilt boundaries. Three types of Shockley partial dislocation lie on (111) with line direction $[10\bar{1}]$: one with its Burgers vector orthogonal to the line direction and two with Burgers vectors at 30° to the line direction. Using Thompson's notation, **Aδ** represents the 90° Shockley (**b**=1/6$[\bar{1}\,2\bar{1}]$) and **Bδ** and **Cδ** represent the two 30° Shockleys (**b**=1/6$[2\bar{1}\,\bar{1}]$ and 1/6$[\bar{1}\,\bar{1}\,2]$, respectively). We choose a vector, $\mathbf{v_A}$, corresponding to a periodic length in crystal A lying parallel to the resulting interface, and then populate each of the (111) planes intersected by this vector with a single Shockley partial dislocation to produce a periodic array of dislocations. The net Burgers vector of the array is the vector sum of the individual Shockleys:

$$\Delta\mathbf{b_A} = n_{A\delta}\mathbf{A\delta} + n_{B\delta}\mathbf{B\delta} + n_{C\delta}\mathbf{C\delta} \tag{2.1}$$

where n_i (i=Aδ, Bδ, Cδ) is the number of each invidual type of dislocation in the array.

For example, (as is discussed in greater detail in section 2.2) FCC Σ=3 {112} boundaries are well described by a periodic dislocation array composed of a 90° Shockley and two 30° Shockleys (*i.e.* ...**Aδ Bδ Cδ**...). Here, the net Burgers vector of the array is zero, and the change in orientation effected by the array is due solely to the twinning operation. We can describe this twinning reorientation (corresponding to a 70.53° rotation about the <110> axis) by a rotation matrix, **R,** that transforms a vector from the initial crystal A to the newly twinned crystal, B. For a general <110> axis, <uvw> (expressed as a unit vector), and for the specific $[\bar{1}01]$ axis used in this paper, **R** is given by (*e.g.*, Forwood and Clarebrough, 1991):

$$\mathbf{R} = \frac{1}{3}\begin{pmatrix} 1+2u^2 & 2uv+2\sqrt{2}w & 2uw-2\sqrt{2}v \\ 2uv-2\sqrt{2}w & 1+2v^2 & 2vw+2\sqrt{2}u \\ 2uw+2\sqrt{2}v & 2vw-2\sqrt{2}u & 1+2w^2 \end{pmatrix} = (\text{for } \tfrac{1}{\sqrt{2}}[\bar{1}01])\ \frac{1}{3}\begin{pmatrix} 2 & 2 & -1 \\ -2 & 1 & -2 \\ -1 & 2 & 2 \end{pmatrix} \tag{2.2}$$

In general, however, the net Burgers vector of the dislocation array will be non-zero. Thus, in addition to twinning the crystal, the dislocation array also introduces a shape change, which adds a second component to the misorientation across the interface (see figure 2-1). Specifically, for a Shockley partial dislocation array with net Burgers vector $\Delta\mathbf{b_A}$, the periodic interfacial vector $\mathbf{v_A}$ will be transformed to a periodic vector $\mathbf{v_B}$ in the new crystal B according to the relation:

$$\mathbf{v_B}=\mathbf{R}(\mathbf{v_A}-\Delta\mathbf{b_A}) \tag{2.3}$$

If both $\mathbf{v_A}$ and $\mathbf{v_B}$ are specified, equation 2-1 can be rearranged to give $\Delta\mathbf{b_A}$:

$$\Delta\mathbf{b_A} = \mathbf{v_A} - \mathbf{R}^{-1}\mathbf{v_B} \qquad (2.4)$$

By combining equations 2.1 and 2.4, and allowing only one dislocation per {111} plane intersected by the periodic interfacial vector, it is possible to solve for the distribution of Shockley partials representing a specific bicrystal orientation and interface plane. To illustrate, Table 2-1 summarizes the sets of Shockley partial dislocations derived from this scheme to the describe several <110> tilt boundaries.

Table 2-1. Crystallographic parameters and resulting dislocation sequences describing several FCC $[\bar{1}01]$ tilt boundaries. θ: misorientation angle; $\mathbf{v_A}$ and $\mathbf{v_B}$: interface period vectors in the A and B crystals; n_{111}: number of {111} planes intersected by the interface period vectors; $\Delta\mathbf{b_A}$: net burgers vector; n_{90}:n_{30}: ratio of 90° to 30° Shockleys in the dislocation sequence. The dislocation sequence is indicated using Thompson's notation with: **Aδ** (90°): **b**=1/6$[\bar{1}\,2\,\bar{1}]$; **Bδ** (30°): **b**= 1/6$[2\,\bar{1}\,\bar{1}]$; **Cδ** (30°): **b**=1/6$[\bar{1}\,\bar{1}\,2]$.

Boundary	θ	$\mathbf{v_A}$	$\mathbf{v_B}$	n_{111}	$\Delta\mathbf{b_A}$	Dislocation Sequence	n_{90}:n_{30}
Symmetric:							
$(\bar{1}31)/(\bar{1}\bar{3}1)$ (Σ=11)	50.5°	1/2[323]	1/2[$\bar{3}$23]	4	1/3[$\bar{1}$2$\bar{1}$]	...**Bδ Cδ**...	0
$(\bar{1}21)/(\bar{1}\bar{2}1)$ (Σ=3)	70.5°	[111]	[$\bar{1}$$\bar{1}$1]	3	0	...**Aδ Bδ Cδ**..	1:2
$(\bar{3}53)/(\bar{3}\bar{5}3)$ (Σ=43)	80.6°	1/2[565]	1/2[$\bar{5}$$\bar{6}$5]	8	1/3[$\bar{1}$2$\bar{1}$]	...**Aδ Bδ Aδ Cδ**...	1:1
$(\bar{5}75)/(\bar{5}\bar{7}5)$ (Σ=99)	90.6°	1/2[7,10,7]	1/2[7,−10,7]	12	[$\bar{1}$2$\bar{1}$]	...**Aδ Aδ Bδ Aδ Aδ Cδ**...	2:1
$(1\bar{1}1)/(\bar{1}1\bar{1})$ (Σ=3)	109.5°	1/2[121]	1/2[1$\bar{2}$1]	2	1/3[$\bar{1}$2$\bar{1}$]	...**Aδ**...	∞
Asymmetric:							
$(1\bar{1}1)/(\bar{1}2\bar{1})$	90°	3/2[121]	[$\bar{2}$$\bar{2}$2]	6	1/2[$\bar{1}$2$\bar{1}$]	...**Aδ Aδ Bδ Aδ Aδ Cδ**...	2:1

2.2 The FCC Σ=3 {112} Boundary

Beyond formally representing intergranular misorientation, the importance of the Shockley Partial Dislocation model is that it provides predictive insight into the grain boundary structure. As an example we consider here theΣ=3 {112} boundary, which has now been studied experimentally and theoretically for a number of different FCC metals, and which is of great practical significance since it is commonly found at the tips of annealing and growth twin lamellae. In the next chapter, we will show how the detailed structure of dissociated, three-dimensional boundaries can be understood the lateral separation of the Shockley partial dislocations describing different boundaries.

Dash and Brown (1963) originally proposed that the tips of FCC annealing twins, which generally form as Σ=3 {112} boundaries, would be composed of equal contributions of the three allowed Shockley partials giving a net Burgers vector of zero. This is very different from a deformation twin, which is bounded by dislocations of the same Burgers vector. The specific atomic rearrangements produced by the array of three Shockleys is illustrated in Figure 2-2. Figure 2-2a shows a $[\bar{1}01]$ oriented FCC single crystal. The atoms are shaded black and white to distinguish between their relative heights in the z-direction, which differ by $1/4[\bar{1}01]$. In Figure 2-2b the sequence of three dislocations, **Aδ Bδ Cδ** ..., has propagated across the crystal and up to a defined boundary plane (in this case $(1\bar{2}1)$); the affected atoms are highlighted in grey in Figures 2-2a,b. This operation reverses the stacking of the right (grey) region of the crystal (twinning it).

The structure of the Σ=3 {112} boundary in aluminum has been studied extensively by both experiment and theory (Pond and Vitek 1977; Medlin et al., 1993; Wright and Atlas 1994; Hamilton and Foiles 2002). This interface relaxes such that the {111} planes crossing the interface are offset by approximately $1/3d_{111}$. Σ=3 {112} boundaries observed in gold (Hetherington 1997) and platinum (Ramanathan 2001), and calculated from first principles for nickel (Hamilton 2002) also have a very similar structure. The dislocation model, which is based solely on geometry, can say nothing about this $1/3d_{111}$ relaxation; however, what it does provide information on is the local *topological* arrangement of atoms. In particular, it successfully predicts the kite-shaped arrangement of atoms (as indicated on the figure 2-2b,c) which found in both empirical potential (Pond and Vitek, 1977; Medlin et al., 1993) and first principles calculations (Wright and Atlas 1994; Hamilton and Foiles 2002) for this boundary.

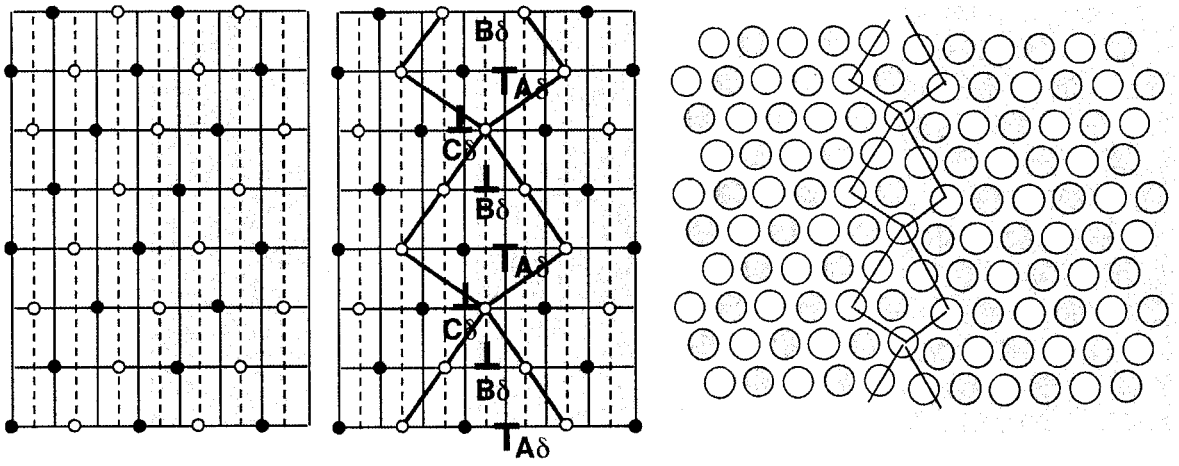

(a) (b) (c)

Figure 2-2. Schematic illustrating how an FCC Σ=3 {112} boundary is formed by a series of three Shockley partial dislocations. (a) The initial [$\bar{1}$01] oriented single crystal . The atoms are shaded black and white to distinguish between their relative heights in the z-direction, which differ by 1/4[$\bar{1}$01]. (b) The atomic arrangements after the series of Shockley partial dislocations (**Aδ**, **Bδ**, **Cδ**) has traversed the right (grey) region of the crystal. (c) An aluminum EAM calculation for the Σ=3 {112} boundary. The dislocation model predicts the topological arrangements of atoms within the kite-shaped structural units.

3. Grain Boundary Dissociation

Experimental observations (Krakow and Smith, 1987; Merkle, 1990; 1991; 1994) and atomistic calculations (Rittner et al., 1996a,b) have demonstrated that many interfaces in low stacking fault energy (SFE) metals relax by emitting stacking faults that extend the structural perturbation of the interface over several planes normal to the interface. In some cases, the arrangement of faults is sufficiently regular that one can identify a distinct, interfacially stabilized, crystallographic phase. For instance, observations and atomistic calculations of Σ=3 boundaries with facets near to {112} show that these interfaces reconstruct in silver and copper to form a narrow (~1 nm) layer of material with the rhombohedral 9R stacking arrangement (Ernst et al., 1992; Wolf et al., 1992) (See Figure 3-1). The 9R stacking sequence, **abc/bca/cab**, can be related to FCC stacking by inserting an intrinsic stacking fault every third close-packed plane, suggesting that low stacking fault energy is a key requirement for the effect. Indeed, observations and calculations of the Σ=3 {112} boundary in aluminum, which possesses a high stacking fault energy, indicate a much more compact boundary structure (Pond and Vitek, 1977; Medlin et al., 1993; Wright and Atlas, 1994).

Though the presence of 9R stacking at Σ=3 interfaces is well understood, less clear are the physical and crystallographic factors that dictate the particular fault arrangement in boundaries of general orientation. In the Σ=3 case, the dislocations that terminate the two FCC/9R interfaces, and that produce the periodic array of stacking faults, lie on a set of close-packed {111} planes that are common to the two FCC crystals on either side of the boundary (Wolf et al., 1992; Carter et al., 1996). Small angular deviations from the Σ=3

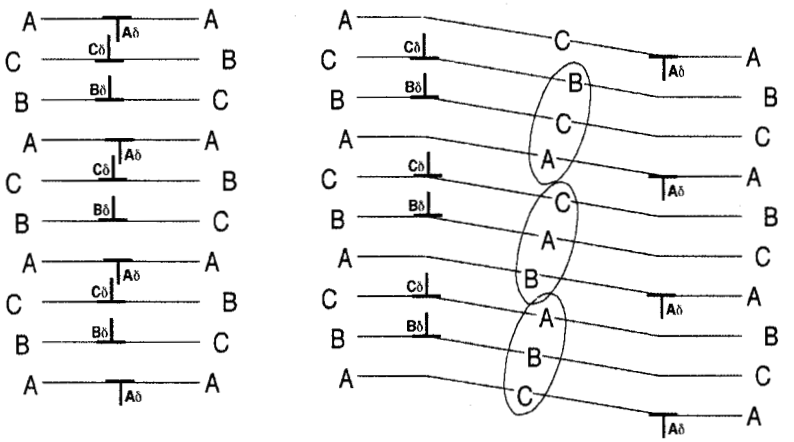

Figure 3-1 Lateral separation of the oppositely signed Shockley partial dislocations that comprise the FCC Σ=3 {112} interface produces a stacking fault every three planes (9R stacking) and plane bending (from Carter et al. 1996).

orientation, and the corresponding breaks in the 9R periodicity, can be explained by variations in the particular sequence of Shockley partial dislocations (**b**=1/6<112>) comprising the two 9R/FCC walls (Hofmann and Finnis, 1994; Medlin et al., 1998; Medlin et al., 1999). It is tempting, therefore, to explore whether the structures at more complex boundaries might also be understood and predicted in terms of similar sets of interfacial dislocations.

In this chapter, we analyze the crystallographic and structural aspects of the interfacial decomposition in two dissociated boundaries in gold. The first boundary we consider corresponds to an intergranular misorientation of approximately 75° about a <110> axis and is formed by the intersection of four {111} twin boundaries. The second boundary we investigate is an asymmetric 90° <110> tilt boundary that is vicinal to {111}/{112}. This boundary configuration is interesting because while it aligns several pairs of low index planes and directions (Carter, 1988), the ratios of periodic lengths in all the parallel directions (with the exception of the shared <110> axis) are irrational. Using the conventional CSL approach to boundary specification, one might classify the ~75° boundary as $\Sigma=3^4=81$ and the 90° boundary as $\Sigma=99$, classifications which provide little insight into the structure of the boundaries. However, as we show below, the interfacial structures at these interfaces can be more simply understood and related to structures found at other <110> tilt boundaries by considering the specific sets of Shockley partial dislocations that account for intergranular misorientation.

3.1 Experimental Procedures

For these experiments we produced boundaries by two methods. The 75° boundary was formed by thermal evaporation of gold onto a <110>-oriented NaCl single crystal substrate (T=300 °C). Because gold possesses a low stacking-fault-energy (32 mJ/m^2), it readily forms growth twins. Under these deposition conditions, the grains of the deposited film inherit either the orientation of the substrate or an orientation that is related to the substrate through a series of 70.53° twinning rotations about the <101> axis. This produces a finite set of well defined and reproducible grain misorientations. The boundary produced by four successive twinning rotations is considered in detail in this chapter. Specimens suitable for high resolution electron microscopy (HRTEM) were prepared by dissolving the NaCl substrate in deionized water, supporting the free-standing gold film on a fine-meshed grid, and then thinning the film to electron transparency by Ar^+ ion milling.

The 90° boundary was fabricated using the thin film "mazed bicrystal" technique (Dahmen and Westmacott 1988; 1991; Pénisson et al., 1999). Specifically, gold was evaporated epitaxially onto [001] germanium producing a microstructure composed of

interlocking <110> oriented grains aligned in two crystallographic variants. The variants are related to each other by a 90° rotation about the shared gold <110> axis, an orientation that aligns {200}Au parallel with {220}Ge. Prior to growth, the germanium substrate was cleaned successively in acetone, methanol, and ethanol, and then etched for several minutes in a 10% HF solution until the surface became hydrophobic. Following a 15 minute long anneal under vacuum (10^{-7} torr, ~550°C) to remove the residual surface oxide, gold (99.99%) was evaporated onto the germanium substrate from a tungsten wire basket (~75Å/sec; T=250 °C). After growth, the substrate was dissolved in a 50%HF:50%HNO_3 solution and the remaining pieces of the film were floated onto fine-meshed gold TEM grids. The supported film was then mounted in an electron microscope heating stage and annealed under the microscope vacuum by gradually increasing the temperature to 680°C over a period of 1 hour.

3.2 Analysis of the Dissociated 75° Boundary

3.2.1 Experimental Results

We begin with an analysis of the 75° boundary. Figure 3-2, an atomic resolution image projected along a <101>-type zone axis, shows the intersection of five grain boundaries. Here, four of the boundaries are {111} twins and possess compact, well-defined cores. By contrast, the fifth boundary, which intersects the junction of four twins and extends from this junction to the top of the image, exhibits a broad, dissociated core with a width of approximately 1 nm. The extent of the spreading can be estimated from the set of nearly horizontal {111} lattice fringes that intersect the two sides of the dissociated boundary. These planes are bent upwards as they cross into the dissociated region from the left and are deflected down as they exit on the right, as indicated in Figure 3-2. By viewing the image from an oblique angle from the left or right one can see this plane bending more easily. Measurements from the image show that the crystal lattices on either side of the boundary are rotated with respect to each other by about 75°, which is close to the ideal misorientation of 77.9° that would be expected for four successive twinning operations.

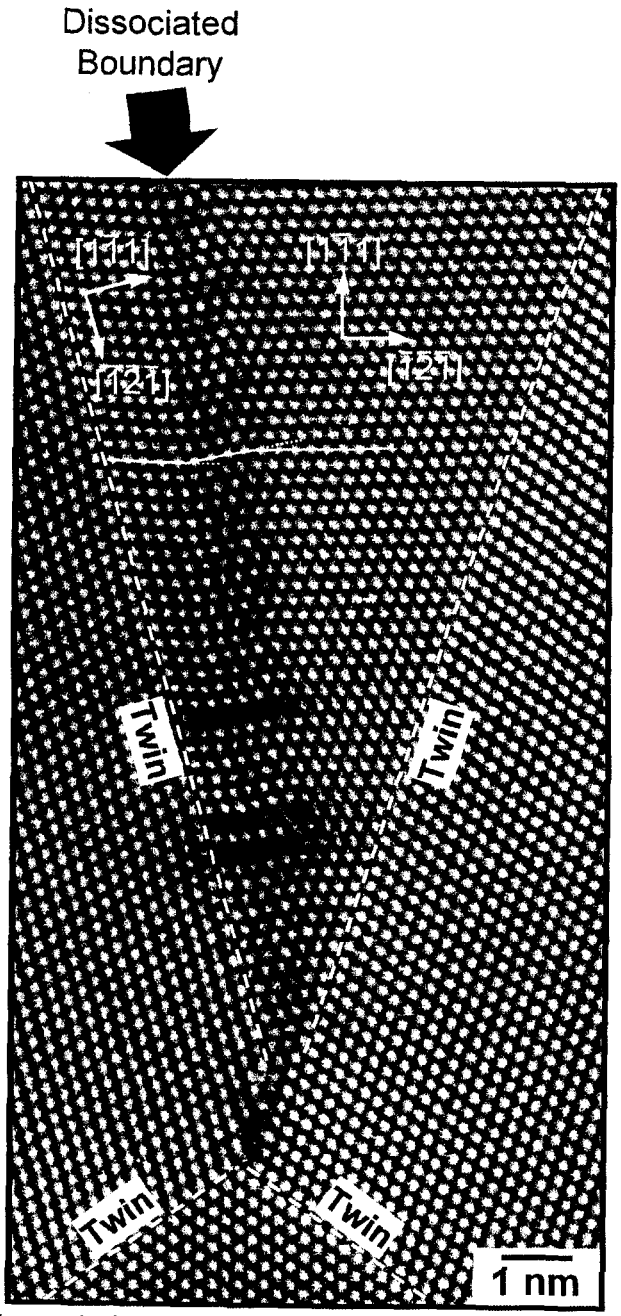

Figure 3-2: High-resolution transmission electron micrograph (HRTEM) showing five grain boundaries: four twins and a dissociated high-angle, tilt boundary described by a 75° lattice rotation about a <101> zone axis in gold. All of the boundaries are viewed edge-on. The horizontal, close-packed {111} planes between the upper twins are deflected as they cross into and out of the dissociated region. This can be observed by viewing the image at an oblique angle from the left or right.

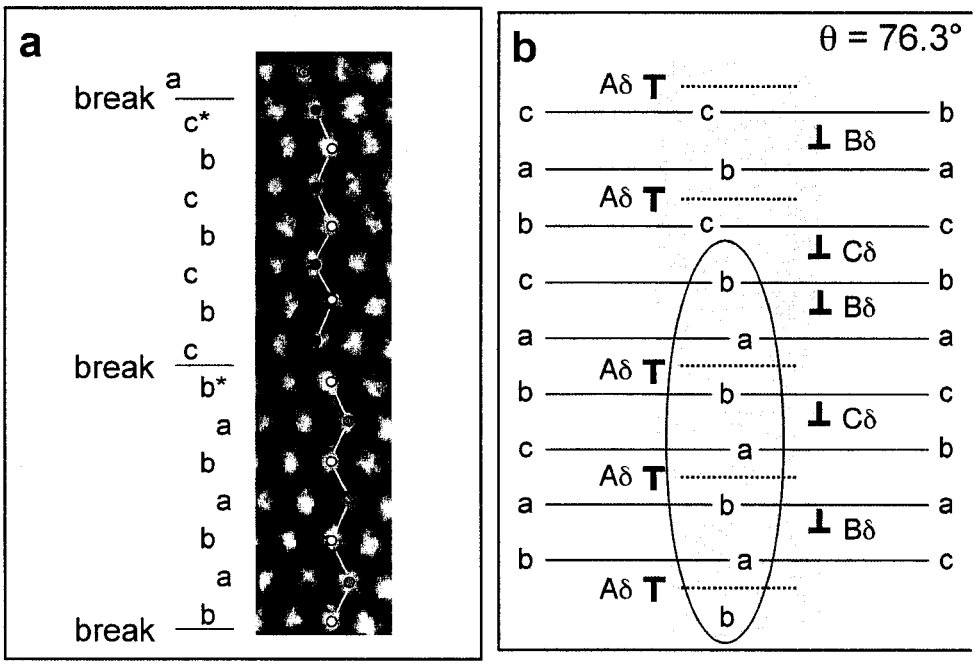

Figure 3-3: a) HRTEM image of a segment of the dissociated boundary shown in Figure 3-2. Solid lines trace out the seven-layer repeat period of hexagonal-close-packed (hcp) stacking. Positions of breaks in hcp stacking are indicated by the dotted lines. Grey, white, and black circles indicate **a**-type, **b**-type, and **c**-type lattice sites, respectively. Asterisks denote atoms that have face-centered-cubic (fcc) coordination. b) A schematic illustration of the separated Shockley partial dislocation array and the location of stacking faults (dotted lines) that yield the observed seven-layer repeat sequence. The letters on the left and right denote the initial stacking of the two grains and the shaded region indicates the extent of the dissociation. The oval marks the stacking sequence identical to that observed in (a). The ratio of 90° (**Aδ**) to 30° (**Bδ**, **Cδ**) dislocations is 3:4, which produces a rotation, θ, of 76.3°.

Details of the atomic arrangements within the dissociated boundary are revealed in a higher magnification image (Fig. 3-3a). Importantly, adjacent close-packed-planes within the dissociated region do not exhibit the stacking expected in a face-centered-cubic (fcc) lattice, but instead exhibit local regions of hexagonal-close-packed (hcp) stacking. In an fcc crystal, neighboring {111} planes follow an **abc** sequence, where the letters signify different low-energy atomic sites. One may envision these sites as corrugations in the surfaces of the atomic planes where each type of layer is offset from the others. In Fig. 3-3a, the shaded dots superimposed on the lattice fringes highlight the observed stacking order. Here, the atoms that would be in the **c** layers (i.e., every third plane) actually reside in **a**-type sites. This produces an **aba** sequence of planes, which indicates hcp order. This stacking breaks

every seven planes where the sequence of layers shifts (e.g. **abc** to **cbc**). The atoms in the plane just below the break point are fcc coordinated, with the atoms after the break continuing as hcp. This seven-plane period repeats over the length of the boundary, a distance of approximately 16 nm, corresponding to about 11 periods.

3.2.2 Analysis of the Shockley Partial Dislocation Distribution

As illustrated in Fig. 3-3b, the boundary is described by a distribution of partial dislocations in a ratio of $n_{90}:n_{30}$ = 3:4, with a sequence of ...**Aδ Bδ Aδ Cδ Aδ Bδ Cδ**... (although we cannot experimentally distinguish between the two types of 30° dislocation, we take them to be in equal proportion, ensuring that their components in the <101> direction cancel and, consequently, that the resulting rotation is a pure tilt about this axis). Separating the 90° and 30° dislocations produces the observed hcp stacking punctuated by a break every seven planes (Fig 2-3b). From the analysis in section 2.1 , the misorientation can be for this dislocation array can be computed to be 76.3°, which compares favorably with the measured rotation of 75°.

3.3 Analysis of the Dissociated 90° Boundary

The boundaries between the 90°-related grains possess two distinct types of facet: {001}‖{110}and {111}‖{112}. The structure of {001}‖{110} facets in this system has been discussed previously by Pénisson and coworkers (1999). Here, we investigate boundaries vicinal to the{111}‖{112}interface.

3.3.1 Experimental Results

Figure 3-4 shows an HRTEM image of one such boundary, which possesses several steps that separate short, 50-75Å, $(1\,\bar{1}\,1)/(121)$ facets. The ratio of periodic lengths in the [121] and $[1\bar{1}1]$ directions is irrational and thus the boundary is incommensurate. This difference in periodicity appears to be accommodated by defects localized at the steps in the boundary. A detailed analysis of the defect content of these types of steps and the manner in which they accomodate the interfacial misfit will be discussed in Chapter 3. We focus here on the regions between the steps, for which the {111} planes on either side of the interface maintain coherency. A higher magnification view of such a region is shown in Figure 3-5. There are two key features to observe in these images. First, as the $(1\,\bar{1}\,1)$ lattice fringes approach the boundary (from the right side), they bend downwards from horizontal through approximately 7°. Second, in the bent region, the image contrast modulates with a period of three $(1\,\bar{1}\,1)$ fringes.

Closer examination of the lattice fringes in the coherent regions shows that the image modulation is associated with a stacking fault every three $(1\bar{1}1)$ planes (indicated by the white lines on the image). The faults are very narrow, extending at most about 10 Å from the interface, and can be seen clearly in Figure 3-5 by viewing the image at an inclined angle and sighting along the set of {111} fringes marked with an arrow. Away from the interface, these {111} fringes are continuous, but close to the interface, they are offset every three planes at the position of the faults. As discussed above, insertion of a stacking fault every third {111} plane corresponds to the 9R stacking sequence.

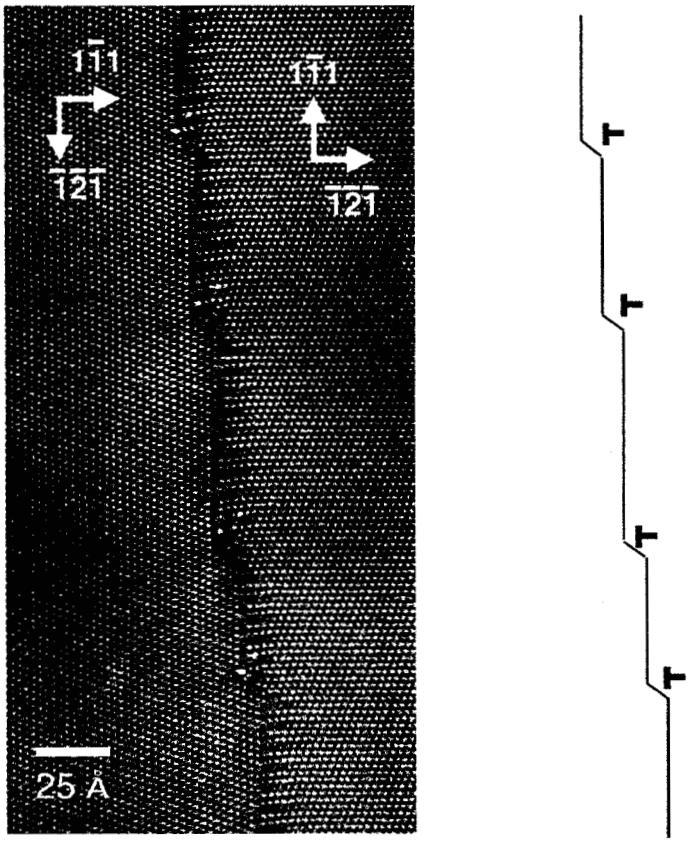

Figure 3-4. HRTEM micrograph showing the boundary between 90° related $<10\bar{1}>$ grains in gold. The boundary is stepped on $\{1\bar{1}1\}/\{121\}$ facets. A modulation of the lattice fringe contrast, with a period of three {111} planes, extends to the right of the interface for a distance of about 10 Å.

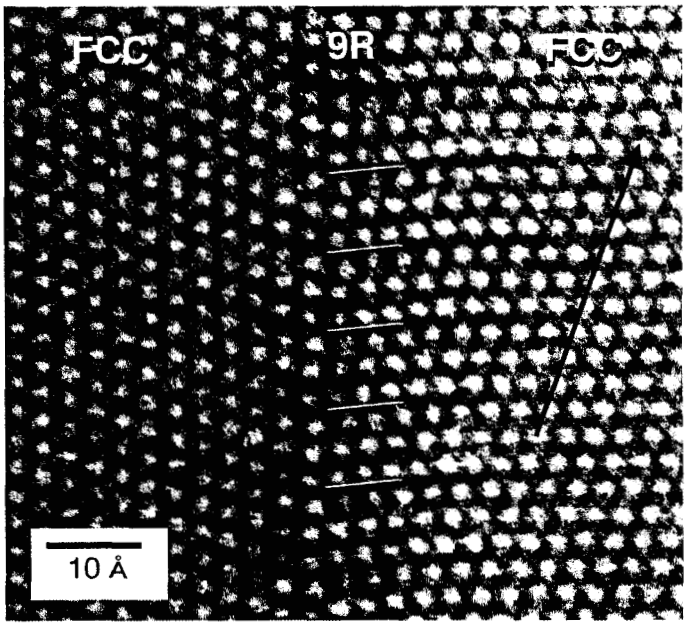

Figure 3-5. HRTEM micrograph showing the dissociated region of the interface. Note the bending of the {111} fringes to the right of the interface. The position of the stacking faults in the dissociated region can be identified by viewing the image at an inclined angle and sighting along the direction of the arrow. The white lines, which are inclined at an angle of 7°, indicate the position and approximate extent of the faults.

3.3.2 Atomistic Simulations

We performed an atomistic simulation to better understand the nature of the dissociation at this boundary. The calculation was based on the Embedded Atom Method (Daw and Baskes, 1983) and employed potentials developed for gold that reproduce an accurate stacking fault energy†. The interface was positioned in the center of a slab geometry, lying parallel to the surfaces of the slab. The slab thickness of ~200 Å was sufficient to ensure negligible interaction between the interface and the free surfaces in the x-

† The gold EAM potential was fit using the functional forms described by A.F. Voter, *et al.*, (1989)in *Atomistic Simulation of Materials: Beyond Pair Potentials,* eds. V. Vitek and D. J. Srolovitz (Plenum, 1989). The parameters from the fit are $D_m = 0.6569$ eV, $R_m = 2.5472$ Å, $\alpha_M = 1.2032$ Å^{-1}, $\beta = 3.1878$ Å^{-1} and $r_{cut} = 5.6$. Also, the r^{10} in the density form is modified to r^8 and the 2^{13} changed to 2^{11}. The resulting properties, with experimental values used for the fit in parentheses (G. Simmons and H. Wang, "Single Crystal Elastic Constants and Calculated Aggregate Properties: A Handbook," MIT Press, Cambridge (1971)), are: Elastic constants (Mbar): c_{11}: 1.858 (1.86), c_{12}: 1.571 (1.57), c_{44}: 0.389 (0.42); Vacancy formation energy (unrelaxed) (eV): 0.97 (0.95); Stacking fault energy 30.7 mJ/m^2 (32 mJ/m^2).

direction. Periodic boundary conditions were chosen in the plane of the slab in order to avoid edge effects. These boundary conditions are straightforward for the z-direction ($[10\bar{1}]$), since the $[10\bar{1}]$ directions in the two crystals are parallel, but introduce a technical complication for the y-direction since the ratio of periodic lengths in the [121] and $[1\bar{1}1]$ directions is irrational. Thus, in mating M 1/2[121] periods on one side of the boundary with N $[1\bar{1}1]$ periods on the other, a bulk strain must be introduced on both sides of the boundary in order to make the total periodic lengths on each side the same. The calculation shown here employs an M/N ratio of 3/2. This choice forces coherence in the interplanar spacing on both sides of the boundary, which approximates the experimental observation of near coherence in the boundary regions between the step defects. The results of these simulations are shown in Figure 3-6. In this figure the shading represents the position of the atoms in the direction normal to the page. The result is a very regular boundary structure that possesses two key similarities to the experimentally observed structure. First, the interfacial region between the two FCC halves has dissociated into a narrow, approximately four atom wide, layer of 9R stacked material. The positions of the stacking faults, which are distributed one to every three planes, are marked by the inclined white lines. Second, the planes are bent in the dissociated layer in a manner similar to that observed experimentally, though at a slightly steeper inclination (~10° rather than ~7°).

The simulation also predicts a relaxation in the z-direction. As indicated by the shading of the atoms, the atoms on the two sides of the right 9R-FCC interface are shifted in the $[\bar{1}01]$ direction (normal to the plane of the figure). This translation, which corresponds to a shift in the z-direction of $1/8[\bar{1}01]$, can be seen more clearly in Figure 3-6b, which shows a projection of the structure orthogonal to that of Figure 3-6a. If this shift is suppressed during the relaxation, the regular boundary structure does not result. Because the experimental observations are sensitive only to the projection of the boundary structure in the imaging direction, it is not possible to confirm the presence of this translation from our existing HRTEM data.

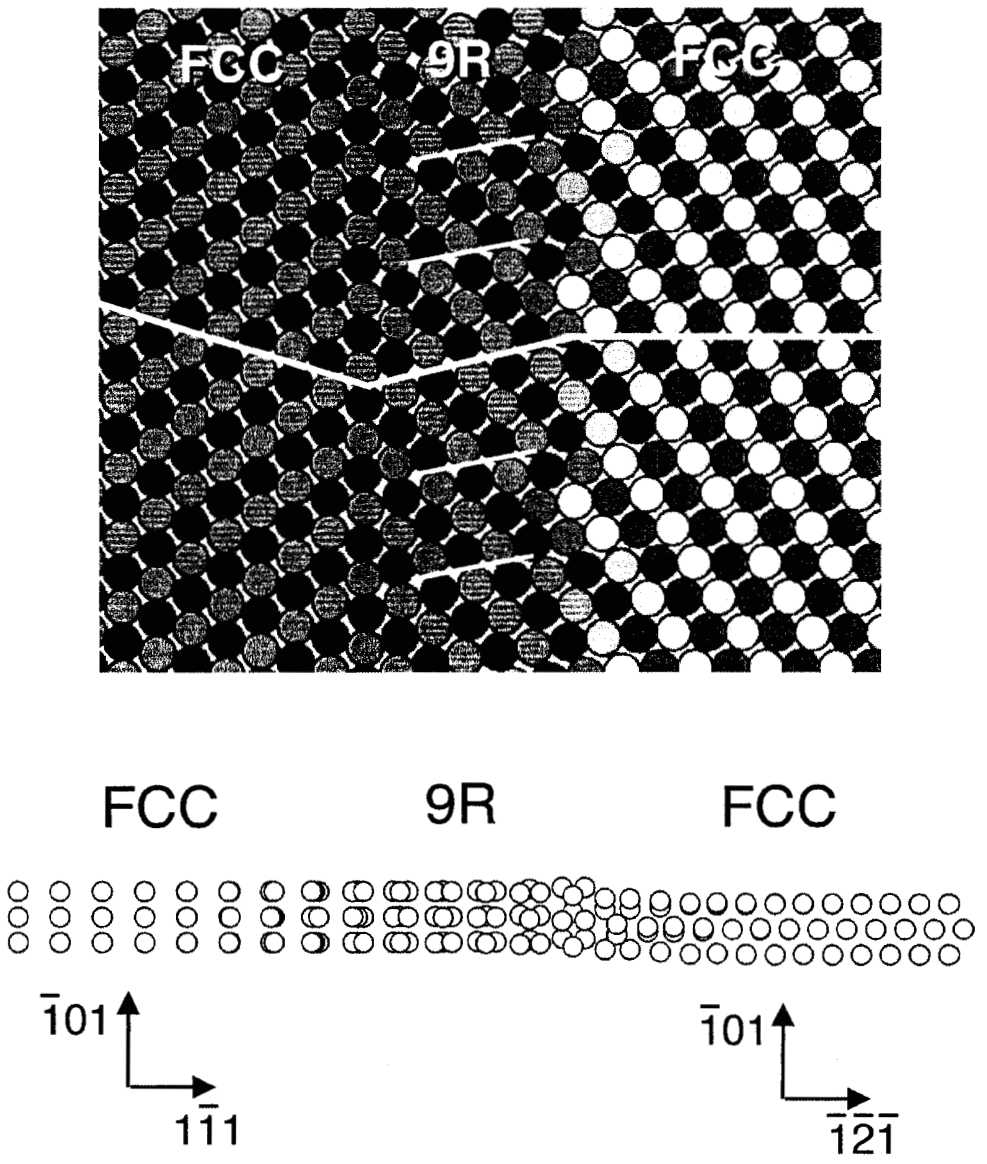

Figure 3-6. (a) $[\bar{1}01]$ projection of atomistic model for $\{1\bar{1}1\}/\{121\}$ interface obtained with an M/N ratio of 3/2. The interfacial region has dissociated into a narrow layer with the 9R stacking sequence. The position of the stacking faults is indicated by the white lines. The shading of the atoms indicates the relative heights of atoms in the z-direction. The atoms on either side of the right-most 9R-FCC interface are offset by $1/8[\bar{1}01]$. **(b)** Same structure as in Figure 3(a) projected orthogonal to the common $[\bar{1}01]$ directions to illustrate the calculated $1/8[\bar{1}01]$ rigid body translation.

3.3.3 Application of the Shockley Partial Dislocation Model to the $\{1\bar{1}1\}/\{121\}$ interface:

The schematic of an undissociated $\{1\bar{1}1\}/\{121\}$ interface shown in Figure 3-8 provides a qualitative explanation of the factors driving the dissociation. The unrelaxed $\{1\bar{1}1\}/\{121\}$ interface is inefficiently packed and possesses a large gap every third plane. The system can increase its packing density by shifting atoms laterally to fill in these openings; however, such a relaxation comes at the energetic expense of introducing faults, which must ultimately limit the degree of the relaxation. Furthermore, the specific type of fault that forms depends on the precise direction of the lateral shifts.

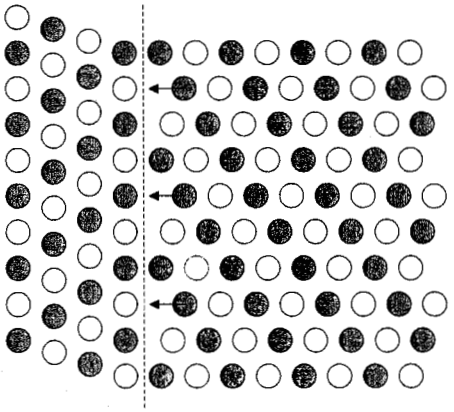

Figure 3-8. Illustration of an unrelaxed $\{1\bar{1}1\}/\{121\}$ interface. The lateral atomic translations to fill in the gaps every three planes leads to the interfacial dissociation by producing a periodic array of faults. For simplicity, the figure is drawn with the the $\{111\}$ planes on the two sides of the interface maintaining registry.

As with the 75° boundary discussed in the previous section, we can determine the specific set of 1/6<112> type dislocations that would be necessary to produce the orientation change across the $90°\{1\bar{1}1\}/\{121\}$ interface by employing the analysis of Chapter 2. However, because this boundary is incommensurate, we must make an approximation. So far, we have implicitly assumed that the number of $\{111\}$ planes intersected by the periodic interface vectors are the same on both sides of the interface. This is strictly true for symmetric tilt boundaries, but is an approximation for an asymmetric boundary such as the $\{1\bar{1}1\}/\{121\}$ interface. For simplicity, we will assume that the $\{111\}$ planes on either side of the boundary maintain continuity. As supported by the experimental observations, this approximation is justified for regions well separated from the interfacial steps, but is clearly inappropriate in the vicinity of these defects, where the lattice disregistry is localized.

Using the coordinate system defined in Figure 3-9, we choose $\mathbf{v_A}$=3/2[121] (left side of the interface) and $\mathbf{v_B}$=[$2\bar{2}2$] (right side). These two vectors represent the shortest combination of periodic lengths for which n, the number of {111} planes intersected by $\mathbf{v_A}$ and $\mathbf{v_B}$, is the same on both sides of the interface. Specifically, $\mathbf{v_A}$ corresponds to three crystal periods in the [121] direction, each of which crosses two {111} planes, and $\mathbf{v_B}$ corresponds to two crystal periods in the [$1\bar{1}1$] direction, each crossing three ($1\bar{1}1$) planes. Thus, a total of six {111} type planes are included in each periodic unit of the boundary. Note that the magnitudes of $\mathbf{v_A}$ and $\mathbf{v_B}$ differ by a ratio of 1.06. Next, we find from equation 3 that $\Delta\mathbf{b_A}$ is equal to 1/2[$1\bar{2}1$]. Finally, from the constraint that $\Delta\mathbf{b_A}$ be distributed amongst six Shockley partial type dislocations, assigned one to each plane, we arrive at a distribution of Shockley partials composed of four 90° dislocations (**Aδ**: **b**=1/6[$\bar{1}2\bar{1}$]) and two 30° dislocations (**Bδ**: **b**= 1/6[$2\bar{1}\,\bar{1}$], and **Cδ**: **b**=1/6[$\bar{1}\,\bar{1}2$]).

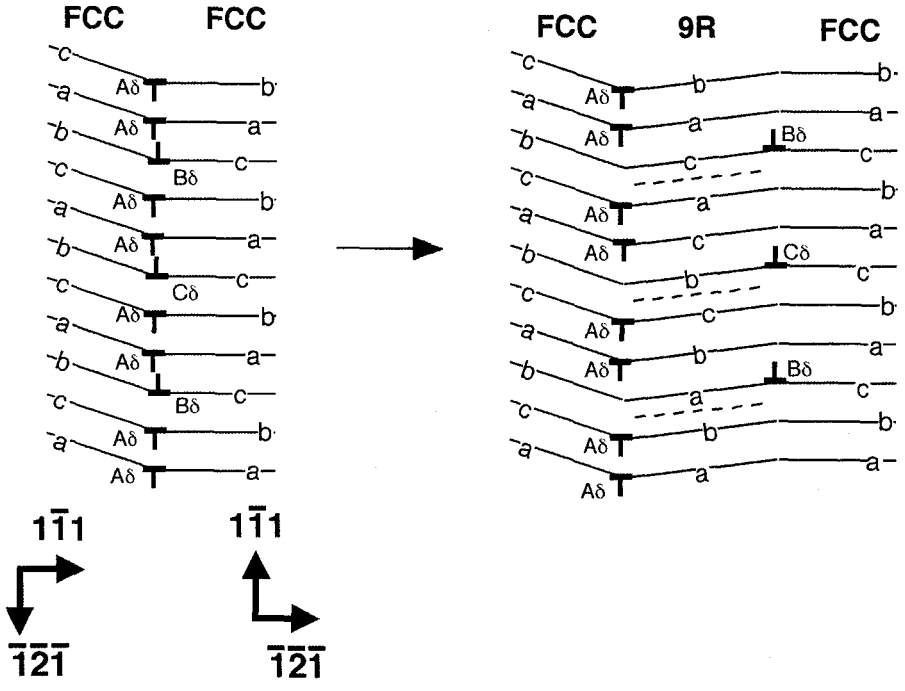

Figure 3-9. Schematic showing the stacking changes that occur at the {1$\bar{1}$1}/{121} interface when the positive 30° Shockleys (**Bδ** and **Cδ**) separate from the negative 90° Shockleys (**Aδ**). Because a stacking fault is produced every three planes, the configuration in the dissociated region is in the 9R stacking arrangement (abc/bca/cab). The isolated array of 30° Shockleys acts as a low angle tilt boundary, bending the {111} planes through 6.7°.

This result points to a remarkable similarity between the dislocation descriptions of the Σ=3 lateral twin and 90°$\{1\bar{1}1\}/\{121\}$ interfaces and explains why both interfaces form a 9R stacking sequence upon dissociation. As discussed in Chapter 2, in the Σ=3 case, the ratio of 90° to 30° dislocations is 1:2, whereas in the $\{1\bar{1}1\}/\{121\}$ interface, this ratio is simply reversed, *i.e.*, 2:1. In the Σ=3 case, the 9R reconstruction occurs when the unlike dislocations (i.e. 90° vs. 30°) separate producing a stacking fault every third close-packed plane. The situation is similar for the $\{1\bar{1}1\}/\{121\}$ interface: separation of the 30° and 90° dislocations will also produce a stacking fault every third plane, provided the 30° dislocations are distributed evenly through the six-plane repeat sequence of the boundary, (*i.e.* in a sequence: ... **Aδ Aδ Bδ Aδ Aδ Cδ** ...). The resulting boundary configuration is illustrated on the right side of Figure 3.9.

This model has an important geometric consequence. Just as the separation of the interfacial dislocations in the Σ=3 case produces a characteristic bending of the close packed planes in the dissociated region (Wolf et al., 1992), so too do the dislocations in the present case. Since the 30° dislocations terminating one side of the 9R region alternate between **Bδ** and **Cδ**, their screw component cancels and the array is effectively a low angle tilt boundary, with the 30° dislocations each contributing an edge component of $1/12[1\bar{2}1]$. For this geometry, the angular change across the wall of 30° dislocations is calculated to be 6.7°, which is consistent with the bending observed experimentally.

3.4 Related Boundaries

The similar behavior of the Σ=3 $\{112\}$ and 90°$\{1\bar{1}1\}/\{121\}$ interfaces underscores the importance of the ratio of 90° to 30° Shockleys in determining the arrangement of faults in dissociated <110> tilt boundaries. Consider the series of boundaries described in Table 2-1. Since the faults arise from the separation of the 30° and 90° dislocations, no dissociation would be anticipated in the limiting cases for which the boundary is composed entirely of 30° dislocations (*i.e.*, the Σ=11 $(1\bar{3}1)/(\bar{1}\bar{3}\bar{1})$ tilt boundary) or 90° dislocations (*i.e.*, the Σ=3 $(1\bar{1}1)/(\bar{1}\bar{1}\bar{1})$ tilt boundary). To our knowledge, calculations of these two interfaces invariably predict compact interfaces, even for low stacking fault energy metals.

The importance of the ratio of dislocation types is further illustrated by considering the case for which n_{90}:n_{30}. is 1:1. As indicated in Table 2-1, this ratio produces the symmetric Σ=43 $(3\bar{5}3)/(\bar{3}5\bar{3})$ 80.6° tilt boundary from a four dislocation long sequence composed of two 90° dislocations (**Aδ**) and two 30° dislocations (**Bδ** and **Cδ**). Rittner and Seidman have calculated the structure of this boundary using a generic, low stacking fault

energy interatomic potential (see Figure 4j of Rittner and Seidman, 1996). Their simulation produced a dissociated structure in which they identified 90° Shockleys terminating stacking faults on every other close-packed plane. This result is consistent with the above description, provided the unlike dislocations are distributed evenly along the boundary (*i.e.*, ...**Aδ Bδ Aδ Cδ**...). We note that such a dissociated arrangement is equivalent to forming a local region of HCP stacking. Thus, our experimental observation of the stacking arrangement in the 75° boundary, combined with the geometrical representation of a grain boundary as a dense array of Shockley Partial Dislocations, confirms this prediction.

Grain boundary dissociation is expected to occur over a range of orientations in low stacking-fault-energy metals and alloys. Our analysis of the long-period interface reported in this work demonstrates that even complex, three-dimensional boundary structures can be treated in a relatively simple geometric context. The success of Shockley partial dislocations in predicting the structure of such dissociated boundaries reflects the tendency of metals that are normally fcc, such as gold, to maintain local, close-packed arrangements that are compatible with the constraints imposed by the surrounding environment. This result helps to establish a physically useful connection between dislocations and grain boundaries, the two most fundamental microstructural elements underpinning the behavior of polycrystalline materials.

4. Accommodation of Grain Boundary Coherency Strain by Interfacial Disconnections

Interfacial dislocations and steps are important in controlling the properties and behavior of grain boundaries, and, thus, their characterization has been central to studies of grain boundary structure. In general, an interfacial line defect may possess both dislocation and step character (e.g. King and Smith, 1980), a configuration that Hirth (1994) has termed a disconnection. Here, we investigate the character of disconnections at a 90° <110> tilt boundary in gold. As discussed in section 3.1, thin film microstructures containing 90°<110> tilt boundaries can be readily fabricated in face-centered-cubic (FCC) metals by epitaxial growth techniques (Dahmen and Westmacott 1988). This has enabled structural studies of boundaries of several different inclinations including a symmetric {557}/{557} facet in aluminium (Dahmen et al. 1990), and asymmetric {100}/{110} (Pénisson et al. 1999, Lançon et al. 2000) and {111}/{112} (Medlin et al. 2001) facets in gold.

The structural relaxations at the {100}/{110} and {111}/{112} interfaces are very different. The {100}/{110} interface is compact with an incoherent interfacial structure (Pénisson et al. 1999, Lançon et al. 2000). In contrast, the {111}/{112} interface exhibits a broad transition region, which is approximately 1 nm wide, over which the boundary is composed of a dense array of stacking faults that are distributed one to every three close-packed planes (this arrangement can be described as 9R stacking) (Medlin et al. 2001). The {111}/{112} facets tend to be fairly short (typically ~5 nm) and are separated by atomic-scale steps. As we show in this chapter, these steps possess dislocation character and play an important role in accommodating coherency strains across the {111}/{112} terraces.

4.1 Defect Characterization

The boundaries in this system meander over length scales of ~10-30 nm, and thereby sample a number of different average inclinations (see Fig. 4-1a), but on a finer scale they are locally facetted on either {111}/{112} or {100}/{110} type planes. Fig. 4-1b shows an HRTEM image of a segment of boundary that is vicinal to {111}/{112}. In general, we observe that the {111}/{112} facets are separated by steps that are only a few atomic planes in height. For instance, in the section of boundary shown in Fig. 4-1b, the steps are two {111} planes high in the lower (μ) crystal. At these terraces, the crystals are locally strained into coherency such that the close-packed planes crossing the interface (specifically, $(111)_\lambda$ and $(1\bar{1}1)_\mu$) maintain continuity, a misfit strain of about 5.7%. Our focus here will be (i) to show how the dislocation content of the steps may be characterised and (ii) to discuss the role these defects play in accommodating coherency strains at the interface.

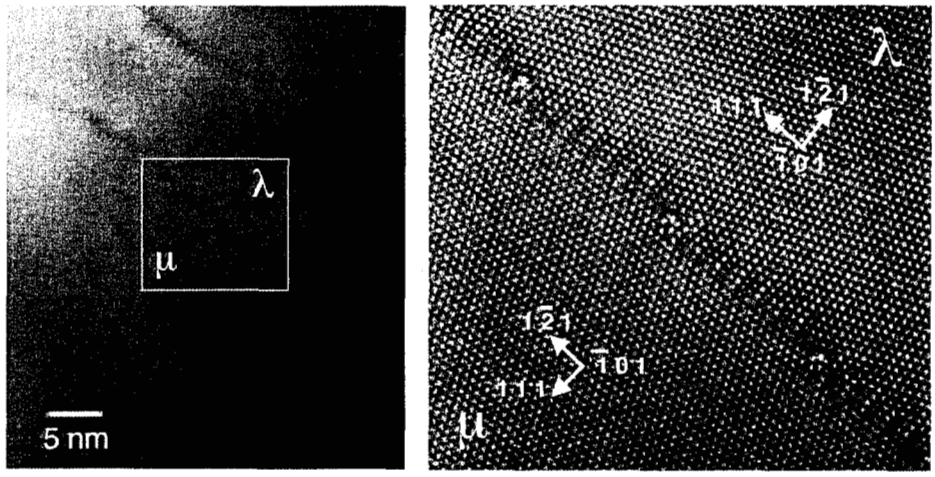

Figure 4-1. **(a)** Bright field TEM image showing the meandering morphology of the 90° <110> boundaries in the Au film. **(b)** Higher magnification image of the indicated region from (a) showing a segment of boundary vicinal to $(\bar{1}\,\bar{1}\,\bar{1})_\mu/(1\bar{2}1)_\lambda$ and the array of interfacial steps.

The definition of dislocation content of epitaxial interfaces between two misfitting crystals depends on the chosen reference state (e.g. Pond and Hirth 1994). If the dichromatic pattern formed by the two, superimposed crystal lattices is selected as the reference, the interface comprises two defect arrays: (i) a continuous distribution of dislocations that ensures coherency between the two crystals via a homogeneous strain and (ii) a set of discrete, "misfit" dislocations, which relieves the coherency strain. Where the misfit is completely relieved, the Burgers vector content of these two arrays is equal and opposite, so only short-range strains arise. Alternatively, with respect to a reference state wherein the two crystal lattices exhibit forced coherency, only misfit dislocations are present. In the present work, this coherent reference state is convenient since its use enables the defect content of individual steps to be measured from experimental images using crystallographic circuit mapping procedures, as have been outlined by Pond and Hirth (1994). In this analysis, we graphically construct a closed loop around a defect of interest and then map this into the reference frame to evaluate the closure failure. In the case considered here, the coordinate transformation relating the crystal lattices in the coherent reference is designated $\mathbf{P}_{coh}$, and describes both the 90° rotation of the two crystal lattices with respect to each other as well as the strain required to force the two crystals into coherency.

These two components generating $\mathbf{P}_{coh}$ can be computed through the following sequence of matrix operations:

$$\mathbf{P}_{coh} = \mathbf{P}_{rel}\mathbf{SAS}^{-1} \tag{4.1}$$

$\mathbf{P}_{rel}$ is the matrix relating the coordinate frames of the two relaxed and unstrained crystals. For the orientation of the crystals as defined in figure 1, this is given by:

$$\mathbf{P}_{rel} = \begin{pmatrix} \frac{1}{2} & -\frac{1}{\sqrt{2}} & -\frac{1}{2} \\ \frac{1}{\sqrt{2}} & 0 & \frac{1}{\sqrt{2}} \\ -\frac{1}{2} & -\frac{1}{\sqrt{2}} & \frac{1}{2} \end{pmatrix} \tag{4.2}$$

A describes a 5.7% uniaxial compression of μ in unit-orthogonal coordinates and is obtained from the ratio of lengths of $[222]_\lambda$ and $\frac{3}{2}[1\,\bar{2}\,1]_\mu$ in their unstrained state ($=2\sqrt{2}/3 = 0.943\ldots$), *i.e.,*

$$\mathbf{A} = \begin{pmatrix} \frac{2\sqrt{2}}{3} & 0 & 0 \\ 0 & 1 & 0 \\ 0 & 0 & 1 \end{pmatrix} \tag{4.3}$$

This strain ensures that the close-packed planes intersecting the interface, specifically $(111)_\lambda$ and $(1\,\bar{1}\,1)_\mu$, maintain registry.

Finally, **S** is a coordinate transformation that converts a vector from unit orthogonal coordinates into μ crystal coordinates ($\mathbf{S}^{-1}$ does the reverse operation), *i.e.,*

$$\mathbf{S} = \begin{pmatrix} \frac{-1}{\sqrt{6}} & \frac{-1}{\sqrt{3}} & \frac{-1}{\sqrt{2}} \\ \frac{2}{\sqrt{6}} & \frac{-1}{\sqrt{3}} & 0 \\ \frac{-1}{\sqrt{6}} & \frac{-1}{\sqrt{3}} & \frac{1}{\sqrt{2}} \end{pmatrix} \tag{4.4}$$

Combining these terms gives $\mathbf{P}_{coh}$ as:

$$\mathbf{P}_{coh} = \frac{1}{18}\begin{pmatrix} (13-3\sqrt{2}) & (-8-3\sqrt{2}) & (-5-3\sqrt{2}) \\ (4+6\sqrt{2}) & (-8+6\sqrt{2}) & (4+6\sqrt{2}) \\ (-5-3\sqrt{2}) & (-8-3\sqrt{2}) & (13-3\sqrt{2}) \end{pmatrix} \tag{4.5}$$

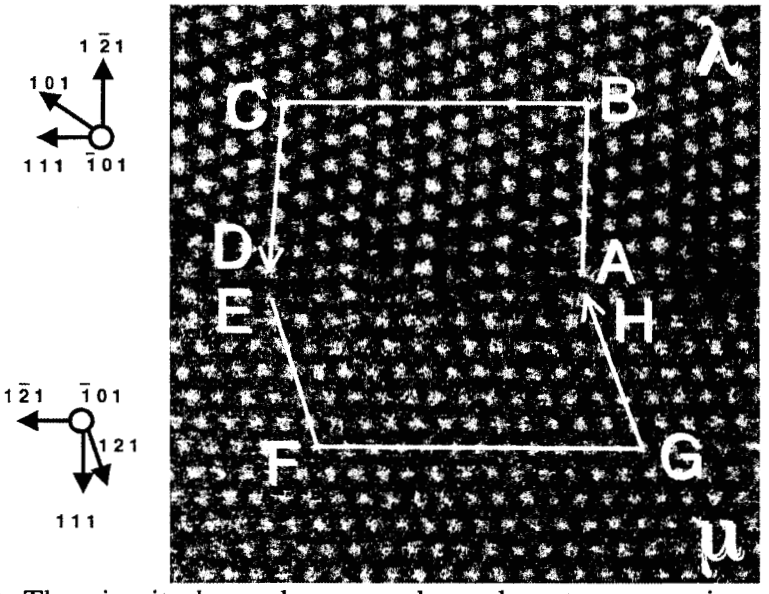

Figure 4-2. The circuit shown here samples only a terrace region. The resulting dislocation content is zero when mapped into the coherent reference frame, $\mathbf{P}_{coh}$.

As a simple example of the use of this coherent reference frame, consider Figure 4-2, which shows a circuit confined to a single {111}/{112} terrace. Here, we designate the upper and lower crystals, respectively, as λ ("white") and μ ("black"). The circuit is divided into separate paths, C_λ and C_μ, in the two crystals. It is important that the two intersections of the circuit with the interface be chosen at crystallographically equivalent points as this ensures that these segments (**DE** and **HA** in this example) cancel in the final vector sum. The dissociated region is taken as being part of the upper (λ) crystal, with the λ circuit starting and ending in this layer at the "faults" that occur every three {111} planes. C_λ, from path **ABCD**, is $4[111]_\lambda$ and C_μ, from path **EFGH**, is $3[\bar{1}2\bar{1}]_\mu$. From the coherent reference state we obtain $\mathbf{P}_{coh}\boldsymbol{C}_\mu = 4[\bar{1}\,\bar{1}\,\bar{1}]$. Consequently, $\mathbf{b} = -(\boldsymbol{C}_\lambda + \mathbf{P}_{coh}\boldsymbol{C}_\mu)^\dagger$ vanishes, as we would expect.

† Here, the sign convention is taken to be **FS/RH** with the line direction out of the page.

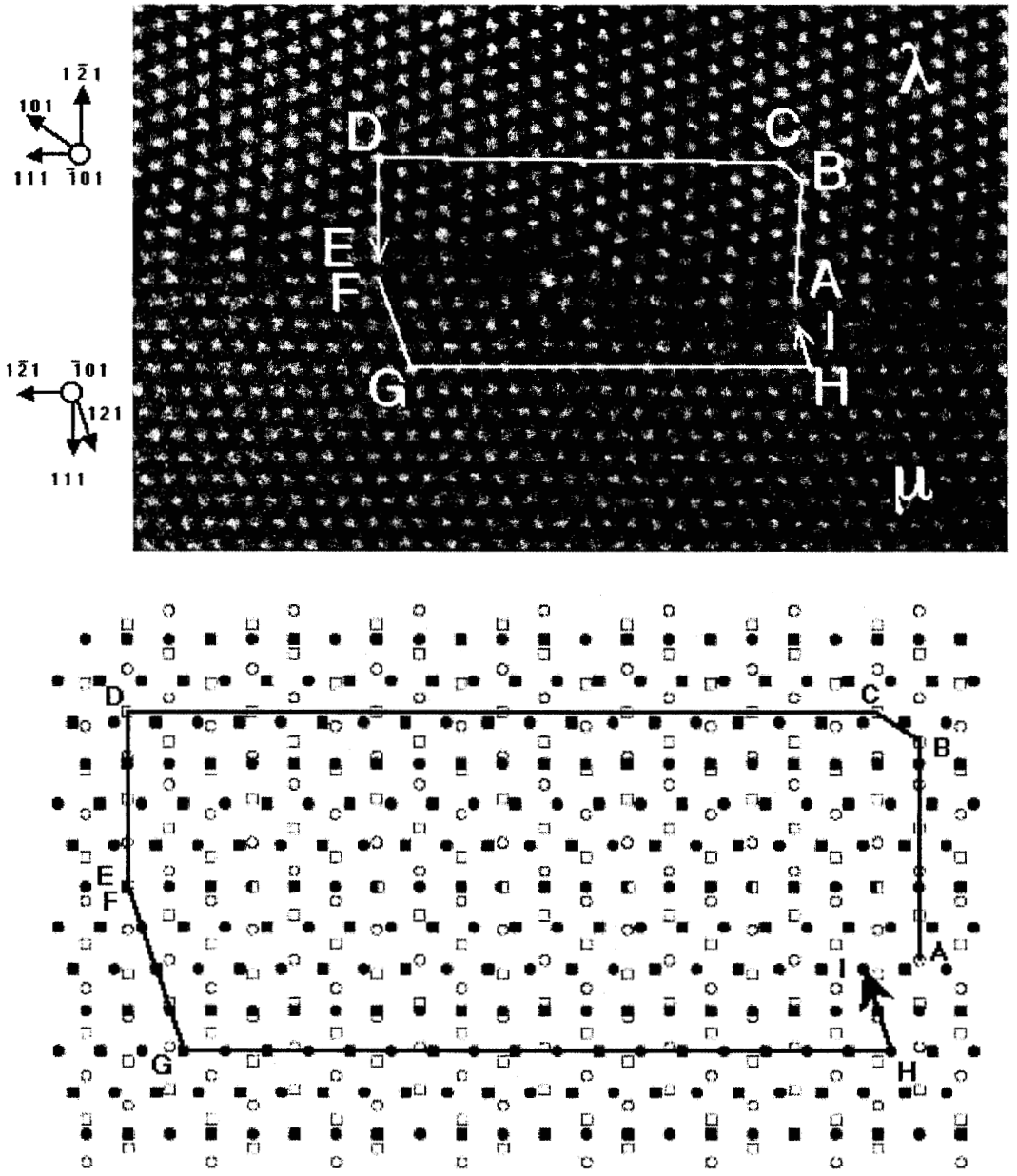

Figure 4-3. **(a)** HRTEM image showing the circuit used to characterize the interfacial disconnection. **(b)** The circuit shown in (a) is mapped onto the dichromatic pattern formed by the superposition of the crystal coordinate frames related by P_{coh} (i.e. the black and white crystals are rotated with respect to each other by 90° about $[\bar{1}01]$ with the black crystal uniaxially compressed by 5.7% along the horizontal axis). Circles and squares distinguish between sites that differ in their z-coordinate (out of the page) by $\frac{1}{4}[\bar{1}\,01]$. The closure failure of this circuit characterizes the dislocation content of the disconnection.

Table 4.1. Summary of the elements of circuit shown in Figure 3. C_λ and C_μ are expressed in the λ and μ coordinate frames, respectively.			
	C_λ		C_μ
AB	$\frac{5}{4}[1\bar{2}1]\pm\frac{1}{4}[\bar{1}01]$	**FG**	$[121]$
BC	$\frac{1}{2}[101]$	**GH**	$\frac{17}{4}[\bar{1}2\bar{1}]\pm\frac{1}{4}[\bar{1}01]$
CD	$6[111]$	**HI**	$\frac{1}{2}[\bar{1}\bar{2}\bar{1}]$
DE	$[\bar{1}2\bar{1}]$		
Total	$\frac{1}{4}[27,22,27]\pm\frac{1}{4}[\bar{1}01]$		$\frac{1}{4}[-15,38,-15]\pm\frac{1}{4}[\bar{1}01]$

A circuit around the central disconnection of figure 4-1b is shown in figure 4-3a. The individual elements of paths C_λ (i.e. **ABCDE**) and C_μ (i.e. **FGHI**) are summarized in table 4.1. In figure 4-3b, this circuit mapped into the coherent reference frame. Note that both C_λ and C_μ must possess components of $\pm\frac{1}{4}[\bar{1}01]$ in the z-direction, but since the HRTEM image is sensitive only to the projected structure in this direction, the ambiguity in the sign cannot be resolved. For simplicity, we will take these components as oppositely signed and therefore cancelling out, giving a defect with pure edge content. It is conceivable, however, that these components could be of the same sign, in which case the defect would also have a screw component of $\pm\frac{1}{2}[\bar{1}01]$. Evaluating the closure failure of the circuit described in table 4.1 with respect to the coherent reference frame, i.e. $\mathbf{b}=-(\boldsymbol{C}_\lambda+\mathbf{P}_{coh}\boldsymbol{C}_\mu)$, gives the following result, expressed in the λ coordinate system:

$$\mathbf{b}=\tfrac{1}{36}\left[12\sqrt{2}-31,\ \ -24\sqrt{2}+14,\ \ 12\sqrt{2}-31\right] \qquad (4.6)$$

$$=[-0.390,\ -0.554,\ -0.390]$$

Circuits around the other two disconnections shown in figure 4-1b give the same result.

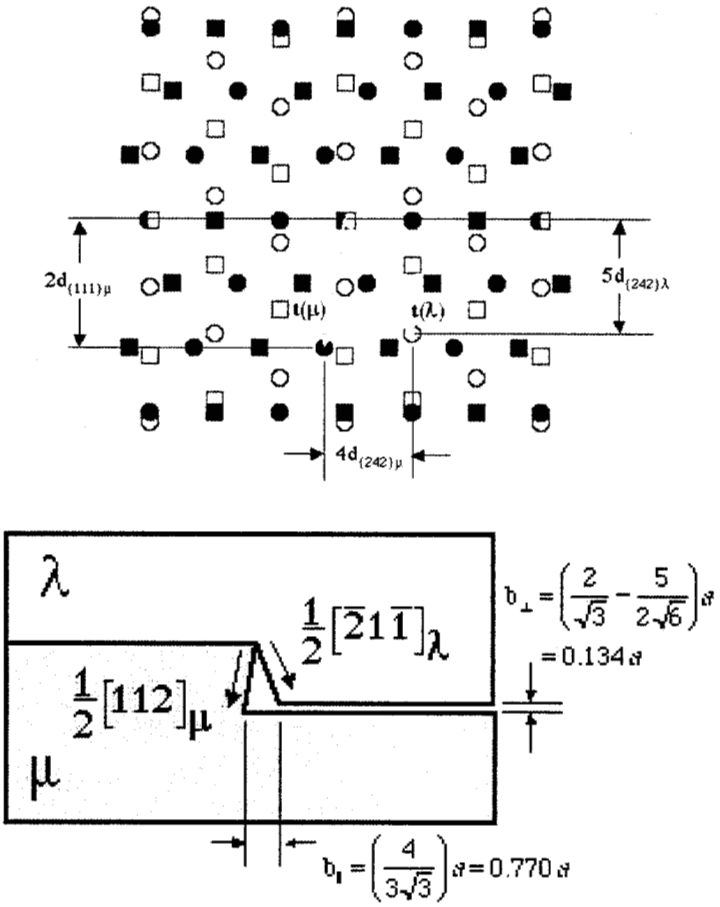

Figure 4.4. **(a)** An enlargement of the dichromatic pattern shown in Figure 3b. $t(\mu)$, in the black crystal, is $\frac{1}{2}[112]$ and is associated with a step of two {111} planes. $t(\lambda)$, in the white crystal, is $\frac{1}{2}[\bar{2}1\bar{1}]$ giving a step of five {242} planes. **(b)** The dislocation content of the disconnection arises from the incompatibility of these two joined surface steps

Table 4-2: Crystallographic parameters describing the disconnection analysed in the present study. The quantities are expressed in the λ coordinate frame in units of the lattice parameter, a.

$\mathbf{t}(\lambda)$	$\mathbf{t}(\mu)$	$\mathbf{b}$	$b_\perp$	$b_\parallel$
$\frac{1}{2}[\bar{2}1\bar{1}]$	$\frac{1}{2}[112]$	$\mathbf{b} = \frac{1}{36}[12\sqrt{2}-31,\ -24\sqrt{2}+14,\ 12\sqrt{2}-31]$ $=[-0.390,-0.554,-0.390]$	$\frac{2}{\sqrt{3}} - \frac{5}{2\sqrt{6}}$ $=(0.134)$	$\frac{4}{3\sqrt{3}}$ $=(0.770)$

The measured dislocation content of these steps is identical with that predicted by the topological theory of interfacial defects (Pond 1989). In general, the Burgers vectors, $\mathbf{b}_{ij}$, of the set of admissible defects at a grain boundary are given by :

$$\mathbf{b}_{ij}=\mathbf{t}(\lambda)_j-\mathbf{P}\mathbf{t}(\mu)_i \qquad (4.7)$$

where $\mathbf{t}(\lambda)$ and $\mathbf{t}(\mu)$ are lattice translation vectors within the white and black crystals, respectively, and $\mathbf{P}$ is the matrix relating the coordinate frames of the two crystals, which we take here as $\mathbf{P}_{coh}$. We select $\mathbf{t}(\lambda)$ and $\mathbf{t}(\mu)$ based on the observed step heights in the two crystals, $h(\lambda)$ and $h(\mu)$, which are given by the perpendicular components of the two halves of the circuit. Specifically, $h(\lambda)=\mathbf{EA}\bullet\hat{\mathbf{n}}_\lambda=-5a/2\sqrt{6}$, (i.e. five $\{242\}_\lambda$ planes), and $h(\mu)=\mathbf{FI}\bullet\hat{\mathbf{n}}_\mu=-2a/\sqrt{3}$ (two $\{111\}_\mu$ planes), where $\hat{\mathbf{n}}$ is the interface normal. Reference to figure 4a then suggests $\mathbf{t}(\mu)$ as $\frac{1}{2}[112]_\mu$ and $\mathbf{t}(\lambda)$ as $\frac{1}{2}[\bar{2}1\,\bar{1}]_\lambda$ giving a Burgers vector in agreement with that deduced from the circuit map. We note that other disconnections with differing step heights and dislocation content have been observed in this sample. An analysis of the full range of defects present in this type of interface will be the subject of further study.

The crystallographic properties of the defect considered here are summarized in table 4-2 and depicted schematically in Fig. 4-4b. The small dislocation component perpendicular to the interface arises simply from the mismatch in step heights of $a(2/\sqrt{3}-5/2\sqrt{6})$. The component parallel to the interface is larger and in λ coordinates possesses a magnitude of $4a/3\sqrt{3}$. Re-expressed in the μ coordinate frame (i.e. by dividing by $2\sqrt{2}/3$) the magnitude of this component is $2a/\sqrt{6}$, which can be interpreted as a deficit of four $(2\bar{4}2)$ planes in the μ crystal.

4.2 Misfit Accommodation

The observed defects appear to be favorable in their role of misfit accommodation. The smallest crystal lattice dislocations possessing a Burgers vector of pure edge character aligned entirely parallel with the interface ($[\bar{1}\,\bar{1}\,\bar{1}]_\lambda$ or $\frac{1}{2}[\bar{1}2\,\bar{1}]_\mu$) would have very large magnitudes (1.73a and 1.22a, respectively) and for this reason are likely to be energetically costly. In comparison, the magnitude of the observed dislocations (0.781a) compares reasonably with that of the smallest possible crystal lattice dislocation (i.e. 0.707a for $\frac{1}{2}\langle 110\rangle$). Yet, because the perpendicular component of the defects is small (0.13a), these defects are able to accommodate the misfit efficiently. We can estimate that the spacing of these defects for complete accommodation of the misfit would be one to every 23.3 $\{111\}$

planes (λ). This is comparable with the dimensions of the {111}/{112} terraces discussed here, which are 25 {111} planes wide.

A further consequence of the finite, though small, perpendicular dislocation component at the steps is that this should introduce a small tilt away from the ideal, 90°-rotated orientation. In the low angle approximation, this tilt is given by $b_\perp / d$, where d is the dislocation separation. For a terrace width of 25 $\{111\}_\lambda$ spacings, we would then estimate a tilt of 0.53° (a clockwise rotation of λ with respect to μ). Experimental measurements from the HRTEM image detect a tilt of 0.97°± 0.08°with the same sense as predicted above. Since the grain orientations are initially dictated by their epitaxial relationship with the germanium substrate, it is likely that this additional tilt relaxation occurs after the film is released from the substrate.

Finally, it is interesting to note the dramatic difference between the structure of the {111}/{112} facets and that of {100}/{110} facets in this same crystallographic system, for which observations and calculations find a fully incoherent structure (Pénisson et al. 1999; Lançon et al. 2000). It is perhaps not surprising that the {100}/{110} facets are incoherent, given the large strains required. For instance, ensuring coherency of {111} planes across the interface by matching <100> with 1/2<110> would require a strain of 29%, while matching <100> with <110> would require strain of 41%. As a consequence, one would expect the γ-surface to be virtually flat, as has been calculated by Lançon (2002), thereby causing dislocations to spread along this boundary. In contrast, the much lower 5.7% misfit at the {111}/{112} facets can be readily accommodated by localised defects, as we have demonstrated here. The comparison between these two cases points to the very important coupling between grain boundary inclination and the particular mode by which incompatibilities between adjacent grains are accommodated.

This analysis helps to explain the role that steps, or more precisely, disconnections, play in accommodating coherency strains at grain boundaries. The particular disconnections observed here, which separate {111}/{112} terraces at a 90° <110> tilt boundary in gold, provide an efficient means of accommodating the 5.7% misfit strain required for coherency at the interface. This analysis also illustrates the importance of specifying the reference state in characterising the topological properties of a disconnection. In particular, by using a coherent reference the dislocation character of the discrete disconnections can be separated from that of the continuous distribution of coherency dislocations.

5. Morphological Evolution of a Faceted Grain Boundary

In this chapter and the next we investigate the development of faceted boundaries and their interaction with dislocations for Σ=3 <111> oriented grains in gold. This system is well suited to experimental studies of grain evolution and dislocation interaction since the crystallography and structure of the boundaries is already well understood. In particular, it is well known that "double-positioning" of epitaxially aligned <111> grains in two 180°-related variants on a surface of three-fold or six-fold symmetry results in a microstructure composed of grains in two twin-related (Σ=3) variants that are separated by $\{11\bar{2}\}$ facets running vertically through the film and forming 120° corners (Dickson and Pashley, 1962; Pashley and Stowell, 1963; Stowell, 1975). Using *in situ* transmission electron microscopy (TEM) experiments, we study how nanometer-scale facets in this boundary migrate and annihilate during annealing to produce a much larger-scale faceted morphology. In the next chapter, we investigate the behavior of dislocations at boundary junctions in this system

5.1 Experimental Procedures

The thin films for this study were produced by depositing gold epitaxially onto [111] oriented germanium single crystals following a procedure similar to that described by Hetherington and coworkers (1997). Prior to deposition, the substrates were first cleaned in acetone and ethanol, immersed in a 10% HF solution until hydrophobic, rinsed in deionized water, dried, and loaded immediately into the deposition chamber. Before commencing each deposition run, the chamber was pumped to a base pressure of approximately 3-5x10^{-8} Torr. Desorption of residual oxide was accomplished by heating the substrates to 550-560 °C and holding for 15 min. Films were typically deposited at rates of 0.4-1.0 nm/sec at growth temperatures between 250 and 280°C to thicknesses between 25 and 50 nm. free-standing, planview specimens for TEM studies were prepared by dissolving the Ge substrate in a solution of either 1 HNO_3: 1 HF or 1 H_2O_2 : 1 HF. The films were then picked up on Au mesh grids. Following deposition, the germanium substrate was dissolved in an acid solution and the film was picked up on a fine meshed gold grid to produce a free-standing, electron-transparent membrane for the subsequent TEM experiments. Two different solutions were employed (1 HNO_3: 1 HF or 1 H_2O_2 : 1 HF) with similar results. Microstructural observations were conducted in a JEOL 2010F transmission electron microscope operated at 200kV. *In situ* annealing experiments employed a Gatan double-tilt heating stage. The two

180°-related orientation variants were imaged separately by tilting the sample close to one of the <112> axes of either of the two variants (a tilt of 19.5° from the [111] axis of the film) and forming a dark-field image using a $\{\bar{1}\,\bar{1}\,1\}$ reflection. Under these conditions only one variant is strongly diffracting. This variant appears bright in the image while the other variant appears dark. Images were recorded digitally as stills or to videotape for subsequent digitization and analysis.

5.2 Morphological Evolution

As illustrated by the grain shown in Figure 5-1a, the $\{11\bar{2}\}$ facets in the as-deposited films are quite small. Analysis of the facet-size distribution from a number of grains shows that over half the total boundary length in the as-deposited films is composed of facets of 25 nm or smaller length (see Figure 5-1b). Annealing dramatically alters this distribution. Following an anneal of 3 hours at 500 °C, the percentage of boundary composed of segments larger than 50 nm has increased relative to the as-deposited film, whereas the percentage of boundary in the smaller facet size ranges has decreased (Figure 5-1b).

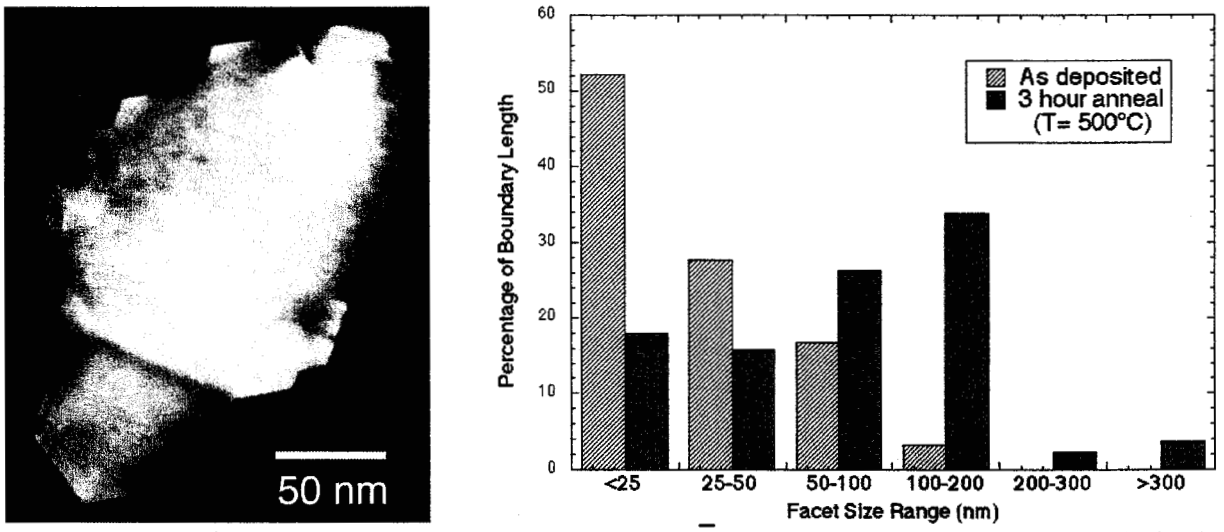

Figure 5-1. (a) Darkfield micrograph showing $\{11\bar{2}\}$ facet steps on an enclosed grain in the as-deposited Au film. (b) Graph shows the proportion of total grain-boundary length as distributed across the range of facet sizes for grains before and after annealing. Prior to annealing, the majority of facets are smaller than 50 nm. With annealing, an increased proportion of boundary length shifts to larger facet size. (As-deposited: n=287. Annealed: n=291)

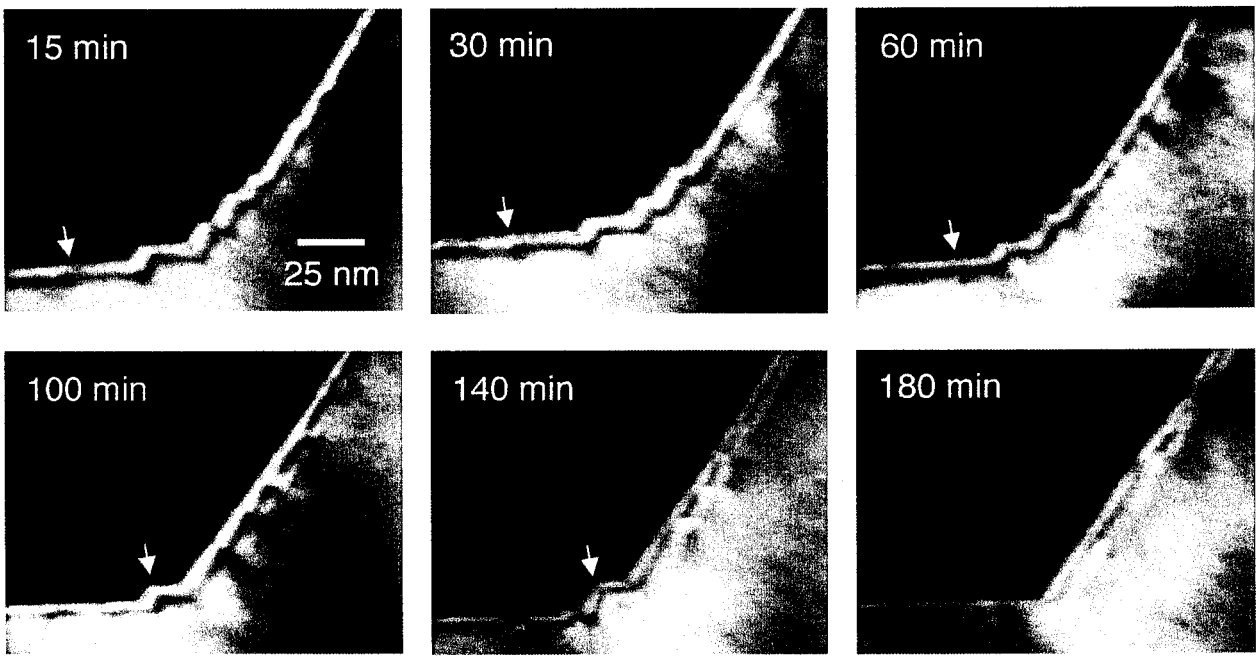

Figure 5-2 Stills taken from video showing motion of $\{11\bar{2}\}$ facets during evolution of boundary corner during annealing (T=490°C).

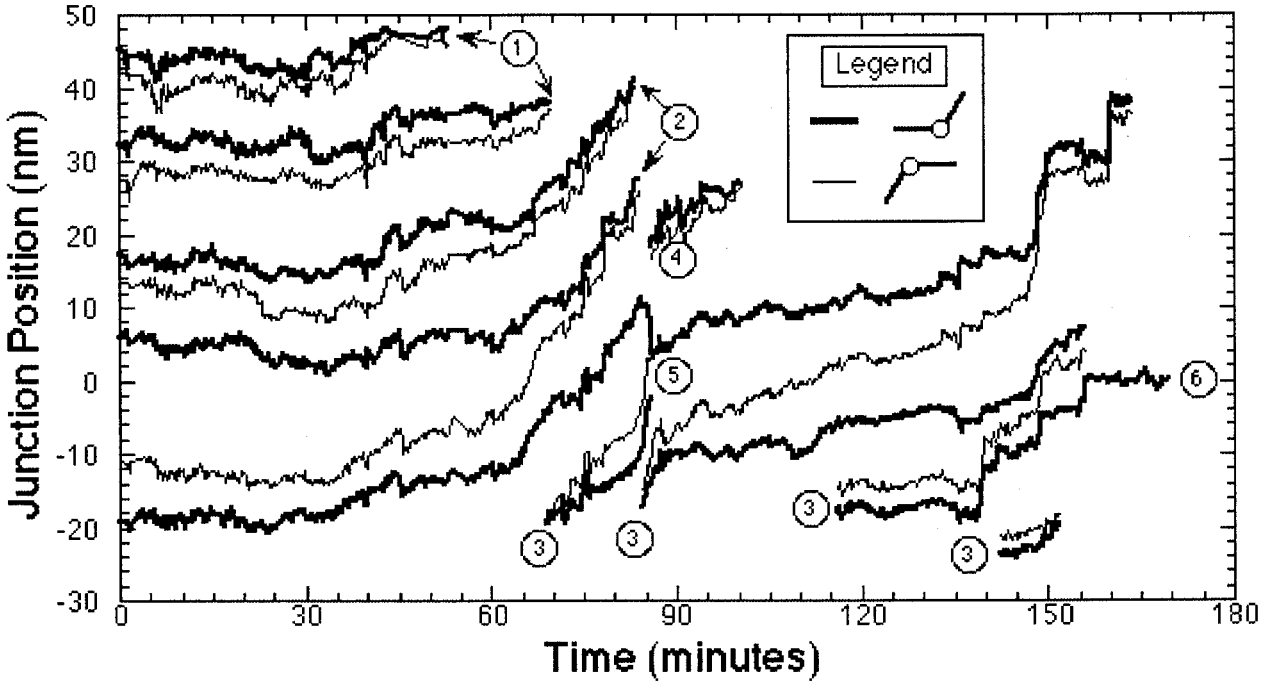

Figure 5-3: Evolution of facet-junction positions with time. Curves are coded according to whether the junction is convex (bold line) or concave (thin line) with respect to the enclosed grain. The numbers refer to events discussed in the text. The positions are expressed as distance along the boundary. Motion in the "positive" direction represents a translation towards the upper right direction in the images shown in Figure 2.

In situ observations show that much step motion occurs during the growth of the larger facets. A series of stills taken during the development of a single facet corner during a three hour long anneal at 490°C are shown in Figure 5-2. The black region in these images is part of a larger grain (approximately 300 nm in diameter) that is completely surrounded by the other 180°-related variant, which appears bright. The junction positions, given as distances measured along the perimeter of the faceted boundary, have been plotted in Figure 5-3 as a function of time. In this plot the positive direction is towards the upper right side of the images as oriented in Figure 5-2, and the zero coordinate is defined with respect to the geometry of the developing corner. Convex corners, which point out of the enclosed grain, are indicated by a heavy line, whereas concave corners, which point into the enclosed grain, are represented by a thin line.

Over time the junctions are eliminated, as in the events labeled **1** and **2** in Figure 5-3, until only a single detectable corner remains (labeled **6** in Figure 5-3). This is by no means a uniform process. In particular, we observe the transitory growth of facets in the vicinity of the developing corner (see the events labeled **3** in Figure 5-3). It is unlikely that the type **3** events represent the nucleation of new junction pairs, since each step forms from a line of contrast on the boundary, which is possibly a pair too closely spaced to be resolved. These contrast features move from the left of the image, grow to a detectable size near the developing corner, and then decrease in size after moving towards the upper right region of the boundary. Note, for instance, the arrowed feature in Figure 5-2 that is barely distinguishable in the initial image but has grown to an obvious corner by 100 minutes.

It is likely that the lines of contrast are secondary grain boundary dislocations (SGBDs). These defects can arise either as a means to accommodate small angular deviations from the exact coincidence orientation or through the decomposition of lattice dislocations into the boundary. A more detailed analysis of the behavior of SGBDs at this type of interface will be given in the next chapter.

In contrast to the type **3** events, a new facet junction pair does form at t=85 minutes (labeled **4** on Figure 5-3). Examination of the video frames (see Figure 5-4) shows that this event is initiated by the intersection of a dislocation with the boundary. In the first two frames the dislocation approaches the boundary. In the third frame a new junction pair, which is circled, has formed. The boundary configuration in the third frame appears to be unstable, since within 12 seconds the junction pair adjacent to the newly formed pair is annihilated (frame 4, figure 4; event **5**, figure 5-3).

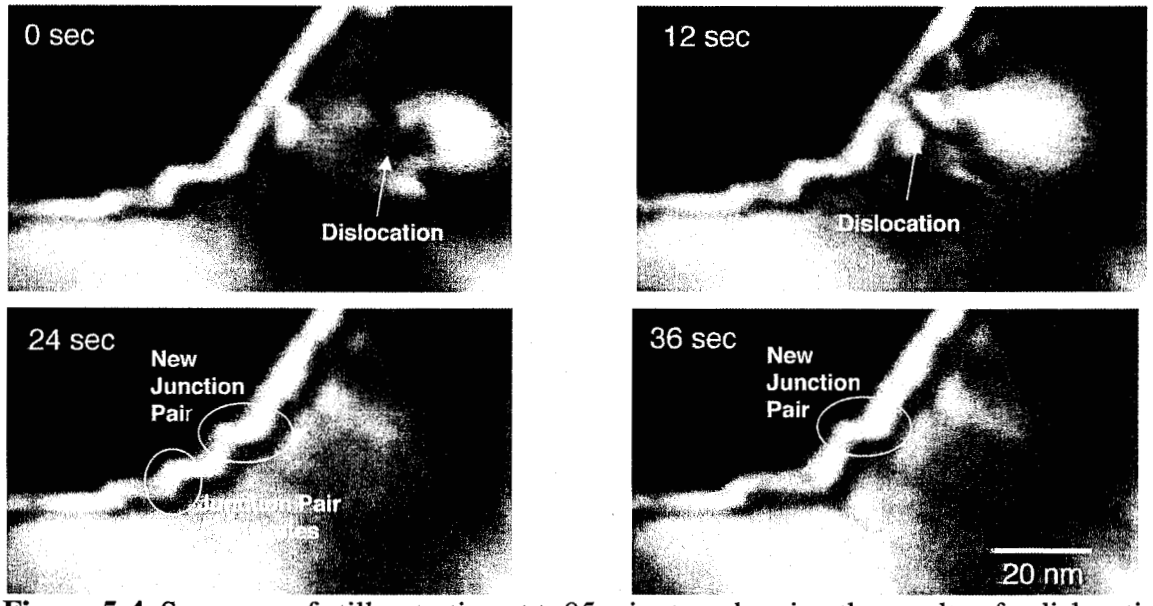

Figure 5-4. Sequence of stills, starting at t=85 minutes, showing the results of a dislocation intersecting the boundary. 0, 12 seconds: The dislocation moves from the right and is about to enter the boundary. 24 seconds: A new junction pair has formed. 36 seconds: The adjacent junction pair has annihilated.

5.3 Motion of "Zero Curvature" Facets

The results of this experiment are surprising in the context of recent models for the evolution of faceted microstructures. Taylor and coworkers have extended the classical capillarity-based descriptions of grain evolution to fully faceted interfaces by employing a non-local definition of weighted mean curvature (Taylor et al., 1992ab). In this approach, facets move as discrete units according to the sign and magnitude of their weighted mean curvature, defined in a crystalline sense. For a two-dimensional polygon, the weighted mean curvature is inversely proportional to the length of the facet and depends on the orientation of the two terminating corners with respect to the Wulff surface. In this description, facets terminated by two convex corners or by two concave corners possess a finite "crystalline" curvature and thus experience a driving force for migration (facet types **a** and **b** in Figure 5-5). In contrast, a facet terminated by corners of opposite sense (type **c** in Figure 5-5) possess zero curvature because no net change in boundary area and interfacial energy results from motion of this interfacial segment. Thus, in computations of grains evolving by crystalline weighted mean curvature, the"zero-curvature" facets remain fixed in position until being fully consumed by facet segments of finite crystalline curvature (*e.g.*, see figure 5 of Taylor et al., 1992a). The result of the present experiment that "zero-curvature" facets are not static, but do in fact move, therefore suggests that other factors, in addition to the reduction of interfacial energy, play a role in the grain evolution of this system.

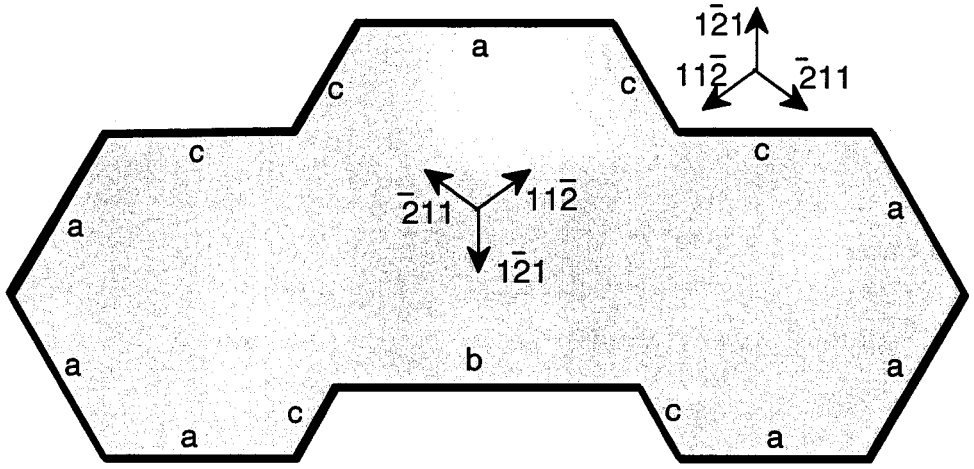

Figure 5-5: Schematic of an enclosed and faceted grain with 120° facet angles evolving towards an hexagonal Wulff shape. Facets labeled **a** and **b** possess finite "crystalline" curvature, since their motion changes the total perimeter of the boundary and, thus, the total interfacial energy. "Zero-curvature" facets, labeled **c**, are bounded by corners of opposite sense and change neither the perimeter nor the interfacial energy when they move.

The key to explaining this behavior may lie in an improved understanding of the facet junctions. In the curvature-based model, no explicit properties are assigned to the junctions--these arise simply as the geometric consequence of joining two facets. However, the atomic relaxations of the interface and at the junction can lead to strain fields at such defects. Indeed, atomic resolution observations of $\Sigma=3\{11\bar{2}\}$ junctions in gold (Hetherington 2000) show a disregistry in the lattice that is due to the discontinuity in rigid-body expansion at the corner of the two adjacent interfaces and should possess dislocation-like character (*e.g.*, Sutton and Balluffi 1995). The unresolved question, then, is whether the resulting strain field leads to any long range interactions between adjacent facet junctions. Aspects of the current experiment are tantalizing in this regard. For instance, the corners appear to follow qualitatively related trajectories--as pairs are annihilated, adjacent junctions move into their place. Similarly, the short time between the nucleation of a new facet-junction pair, following the intersection of a dislocation with the boundary, and the subsequent annihilation of an adjacent junction pair, may indicate that the new junction pair has destabilized the local boundary configuration.

6. Dislocation Emission and Interaction at Grain Boundary Junctions

In this chapter we examine the dynamic behavior of dislocations in the vicinity of a grain boundary junctions. As in Chapter 5, we employ Au Σ=3 thin film bicrystals. As discussed above, the domains in these films are primarily separated by {112} type grain boundary facets. However, in some cases the domains overlap through the thickness of the film, and in these regions the boundary forms on a {111} facet (i.e. a "coherent" twin boundary), parallel to the film surface (see Figure 6-1a). The junction between these two types of boundary provides a very well defined geometry for investigating dislocation interactions and is of practical relevance in understanding the development and behavior of twin boundaries in thin film materials.

A schematic illustration of the topography of one domain in the area of a facet junction is shown in Fig. 6-1b. The Σ = 3 {112} boundaries separate the domains and are perpendicular to the substrate, while the Σ = 3 {111} boundaries result from an overlap of two domains and are parallel to the substrate (Fig. 6-1a). Because of the 120° angle between {112} facets bounding a particular domain, the twin plane forms a 60° angle when viewed in a planview orientation (Fig. 6-1c, Fig. 6-2).

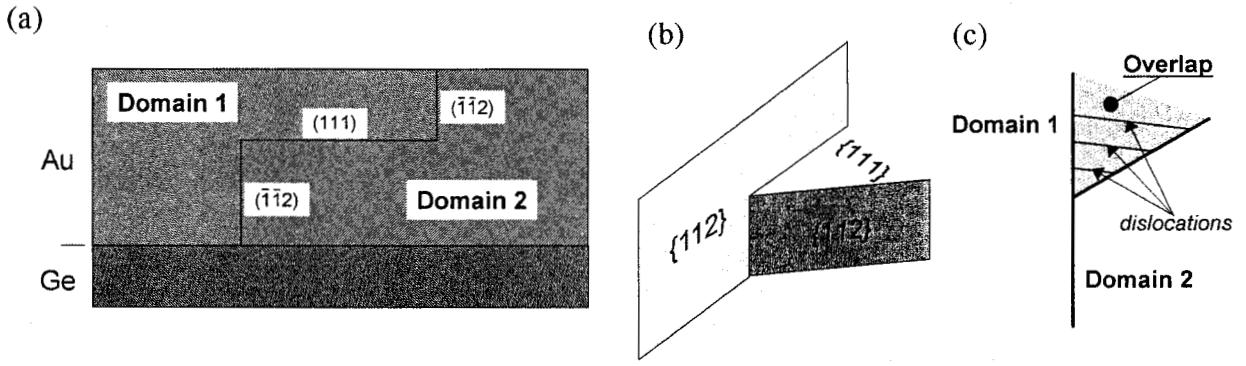

Figure 6-1: (a) Schematic illustration of the Au film crystallography and grain boundaries as viewed along a <110> zone axis. (b) Perspective view showing the geometry around a facet corner in one domain. (c) Schematic of facet corner/twin in planview orientation. Shaded area indicates the extent of the overlap of the two domains.

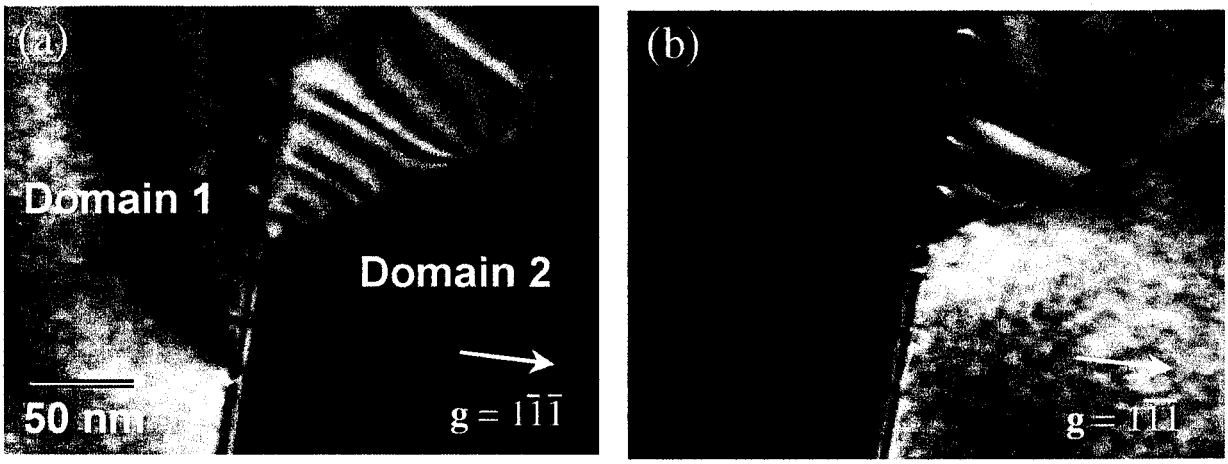

Figure 6-2: Planview dark-field images of the two separate domains imaged using a ($\bar{1}\,\bar{1}$ 1) reflection (sample is tilted ~19.5° from surface normal). (a) Specimen tilted to <112> zone of domain 1. (b) Specimen tilted to <112> zone of domain 2.

Dislocation-like contrast at the overlapping regions (i.e., twin boundaries) of double positioned grains in Au films was observed previously by Stowell (1975), however, little information was provided on the origin and nature of these defects. Our planview transmission electron microscopy (TEM) studies of such regions revealed arrays of uniformly spaced dislocations, as shown schematically in Fig. 6-1c, that appear to emanate from the facet junctions. This configuration was observed frequently and was present in different sample runs. This raises an interesting question: what is the origin of these defects and what is their relationship to the boundaries with which they intersect? In the remainder of this chapter we describe TEM experiments to determine the source of these arrays. Through diffraction contrast measurements, we have determined the Burgers vectors and using *in situ*, hot-stage experiments we have investigated how the array evolves with respect to the facet junctions. From these results, we propose a formation mechanism for the dislocation arrays. Finally, we test the plausibility of this hypothesis through a calculation of the relevant dislocation interaction and line energies.

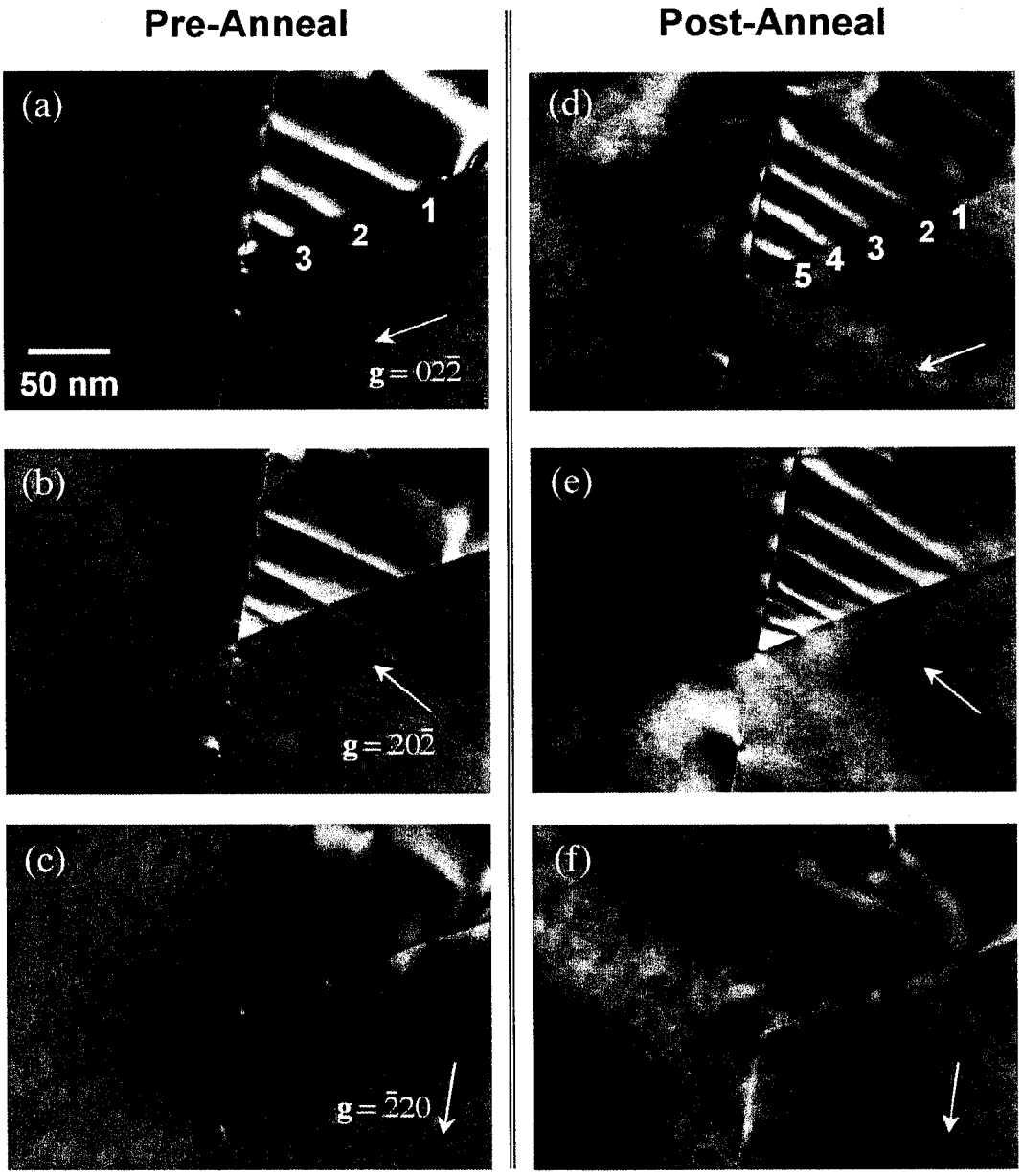

Figure 6-3: A series of two-beam, dark-field images using three {220} reflections prior to the *in situ* experiment (a-c). Dislocation strain contrast is effectively invisible in (c) $\mathbf{g} = [\bar{2}20]$. The same area imaged after *in situ* observation and the emission of two dislocations (**d-f**). The most recently emitted dislocations (**4** and **5**) are effectively invisible under the same diffracting conditions as the previously existing dislocations (**1-3**).

6.1 Character of the dislocations

In order to unambiguously identify overlapping regions, the two orientation variants in the microstructure were imaged separately under different diffracting conditions. Specifically, the specimen was tilted to a <112> zone axis of each of the two domains and dark-field images were formed with the $(\bar{1}\,\bar{1}\,1)$ reflection. Image pairs showing complementary contrast indicate regions where the domains extend completely through the thickness of the film, whereas regions that are bright in both images show overlapping areas that contain a twin. For example, in Fig. 6-2 the central triangular region that appears bright in both images is overlapping, as shown schematically in Figure 6-1b and 6-1c. Contrast arising from the strain fields of the dislocations is also visible in Fig. 6-2. A series of dark-field, planview images taken from a different Au thin film specimen is shown in Fig. 3a-c. The (111) twin boundary in the image is bordered by two {112} facets along <110> directions and initially contained three, straight dislocation segments separated by ~20 nm. The line direction of these dislocations is essentially parallel to $[10\bar{1}]$, creating an acute angle of 50-60° with the bounding facets. These dislocations either originated during film deposition or from the 400 °C anneal. The uniform line contrast along the line direction agrees with the expectation that the dislocations run parallel to the film surfaces.

Next, a $\mathbf{g} \bullet \mathbf{b}$ analysis was conducted to determine the Burgers vector of the dislocations. As shown in Fig. 6-3, the dislocation contrast effectively vanishes for $\mathbf{g} = [\bar{2}20]$, but is strong for the remaining two {220}-type reflections. This result excludes the crystal lattice dislocations that would lie in the (111) plane ($\mathbf{b} = \pm 1/2[10\bar{1}]$, $1/2\ \pm[1\,\bar{1}\,0]$, and $1/2\ \pm[01\,\bar{1}]$). The contrast is consistent with dislocations possessing a Burgers vector of $\mathbf{b} = 1/6[\bar{1}\,\bar{1}\,2]$, which is a displacement shift complete (DSC) vector of the $\Sigma = 3$ boundary. Since all the dislocations vanish simultaneously, the Burgers vectors are parallel. Systematic observations of the shift in the location of contrast from the dislocations while imaging using $+\mathbf{g}$ and $-\mathbf{g}$ diffraction conditions revealed that the dislocations have the same sign.

These dislocations cannot simply terminate at the adjacent {112} facets. To determine the dislocation configuration in these boundaries, the specimen was tilted away from film normal, inclining the boundary to the electron beam. As illustrated in Fig. 6-4, the dislocation segments lying on the twin have threading segments that extend from the point of intersection of the horizontal twin with the vertical facet and terminate at the film surface.

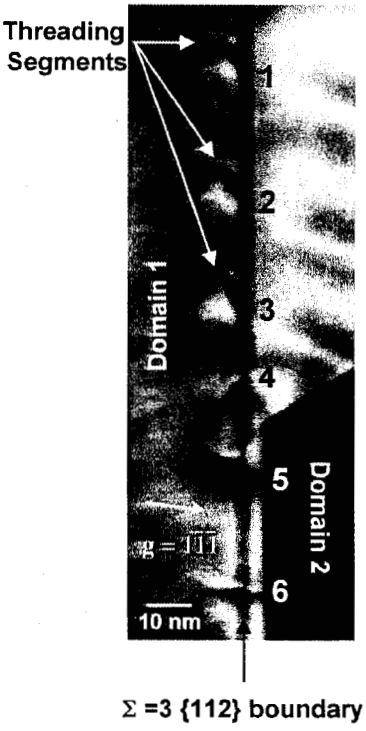

Figure 6-4: A high magnification planview, dark-field image showing detail in a {112} boundary bordering a horizontal twin. The {112} boundary was inclined relative to the electron beam by tilting the specimen. The twinned area is located in the upper right quadrant of the image. Threading segments extend from the edge of the twin to the film surface.

Also apparent in Fig. 6-4 are two threading dislocations, labeled **5** and **6**, that lie on the {112} facet *ahead* of the junction. Our observations show that threading dislocations are commonly observed in this geometry. For example, careful examination of Fig. 6-3 shows localized contrast features ahead of the junction in this case as well. Because threading dislocations in a [111]-oriented specimen would be imaged end-on, this contrast in Fig. 6-3 and Fig. 6-5 is likely arising from relaxations at the intersection of the dislocations with the foil surface (Tunstall et al., 1964).

6.2 Origin of the dislocations

In order to establish the origin of the dislocations in the twin and to examine further the interactions between dislocations, we conducted an *in situ* heating experiment. The specimen was heated to ~550 °C and held isothermally while recording images to videotape. A chronological sequence of frames captured from the video is shown in Fig. 6-5. Initially, feature **4** moved away from the junction to the right (a-c). Subsequent frames (d-f) show that feature **5** climbed along the {112} boundary and passed the facet corner forming a new segment in the twin plane. Compared with the initial image, the four previously visible dislocations have shifted to the right, maintaining a uniform spacing of ~25 nm. A $\mathbf{g} \bullet \mathbf{b}$ analysis performed after cooling the specimen to room temperature (see figs. 6-3d-f) confirmed that the newly emitted dislocations exhibited the same contrast behavior as those

already in the boundary, again indicating that the Burgers vectors of all of the dislocations were parallel and had the same sign. The emission process was reproduced in several separate experiments on different areas and samples. Thus, the *in situ* TEM results demonstrate conclusively that the dislocation arrays observed on the horizontal {111} twin facets result directly from the migration of the threading dislocations that lie on the vertical {112} facets. Because the dislocation line and motion is on the horizontal {111} twin plane these dislocation segments are glissile and migrate by gliding.

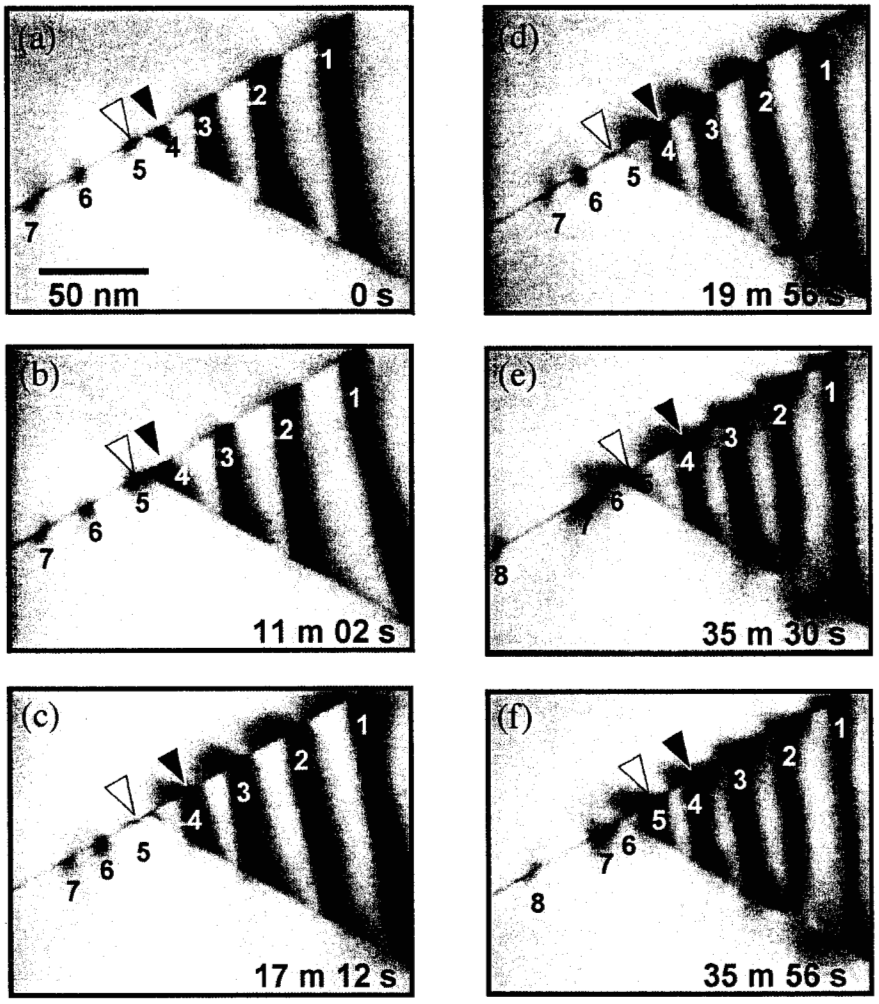

Figure 6-5: Series of video frames obtained from a 50 nm-thick Au film annealed at 550-600 °C showing the movement and emission of two dislocations (numbered 4 and 5) from a {112}-facet perpendicular to the film surface into a {111}-twin boundary parallel to the film surface. Note that this is the same boundary as in Fig. 6-3, but rotated.

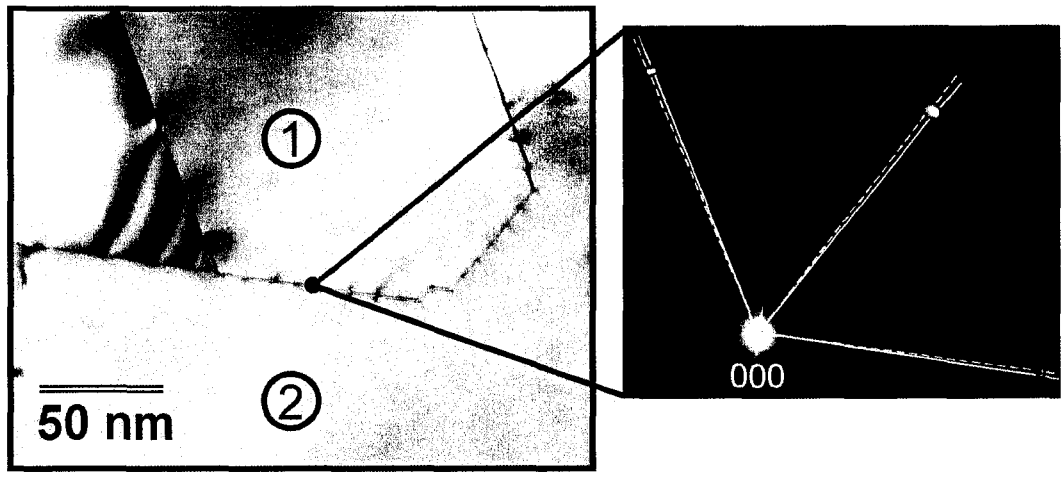

Figure 6-6: Bright field image and SADP obtained from a different area of the sample showing an array of SGBDs in the boundary between domains 1 and 2. An enlarged quadrant of the diffraction pattern taken with the selected area aperture positioned over the boundary resulted in two rotated sets of (111) spots. The spots arising from domain 1 are indicated with solid lines and the spots from domain 2 are indicated with dotted lines.

6.3 Interdomain Misorientation

The threading dislocations are expected to accommodate deviations from the exact Σ=3 orientation. For an array of 1/6 $<\bar{1}\,\bar{1}2>$ threading dislocations, for which the Burgers vectors are orthogonal to the facet, the domains along the {112} facets should deviate by a pure tilt rotation. Such dislocations would have to migrate by climbing as will be discussed in detail later.

To ascertain the magnitude of the inter-domain misorientations, several grain boundaries adjacent to facet corners, similar to the one in found in Fig. 6-2, were surveyed. A bright-field image of a typical area is shown in Fig. 6-6, revealing uniformly spaced features that delineate the domain boundary. An enlarged quadrant of the corresponding SADP obtained with the aperture positioned over the grain boundary showed two sets of spots (one set from each domain) indicating an in-plane rotation between the two domains. For the boundaries examined, the deviation from perfect coincidence ranged from 0.1° to 1.6° with a mean value of 0.7°.

Using the measured distances between dislocations and the respective rotation angles from all of the boundaries to calculate the Burgers vector resulted in a mean value of **b** = 1.7 ± 1.0 Å. The large uncertainty associated in this number results from the experimental error (± 0.1°) in measuring the angles between domains. Also, in some cases the dislocations were not uniformly spaced. For comparison, the magnitude of the Burgers vectors for a/6 <112>, a/3<111>, and a/2 <110> dislocations in Au are 1.665 Å, 2.354 Å, and 2.884 Å, respectively. The closest match between measured **b** and the magnitude of an *a*/6 <112>-type dislocation

is consistent with the expected DSC dislocation for this boundary type as mentioned earlier. This data alone does not allow a definitive conclusion to be drawn about the Burgers vector of the SGBDs. However, when taken in context with the TEM results and the crystallography of the sample, it supports the idea that the observed features in the {112} boundary are SGBDs of the type a/6 <112> accommodating small rotations between domains.

From the analyses described above, we can now summarize the configuration of the dislocations observed in the microstructure (Fig. 6-7). The Au bicrystal film is composed of faceted $\Sigma = 3$ {112} boundaries perpendicular to the substrate and horizontal $\Sigma = 3$ {111} twin boundaries that are parallel to the substrate. Threading SGBDs in the {112} facets initially accommodate inter-domain rotational misorientations introduced during film growth. During annealing, these dislocations are emitted into the twin planes and form glissile segments, while the threading segments terminate at the top and bottom surfaces of the film. Over time, the dislocations migrate along the twin and away from the facet corner. Repetition of this process forms arrays of grain boundary dislocations on the twin plane. The possibility of interactions between the dislocations driving emission and migration is addressed in the next section.

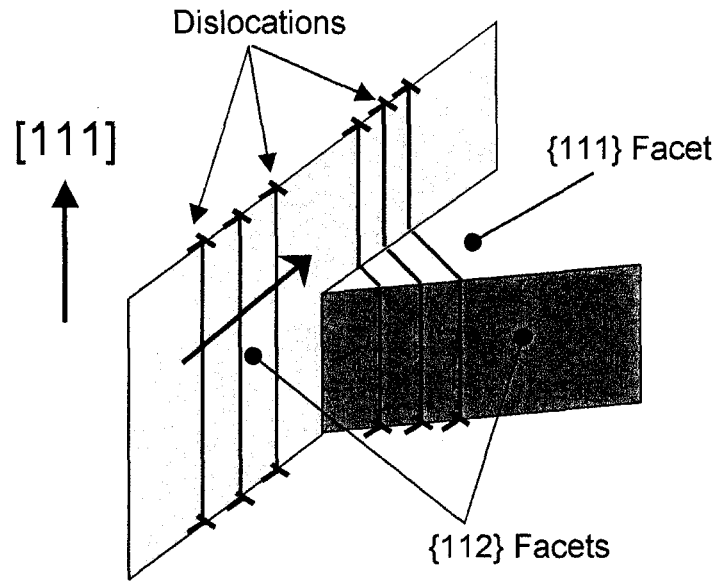

Figure 6-7: A schematic illustration depicting the arrangement of dislocations around a facet junction and a twin boundary between two overlapping domains.

6.4 Forces Driving the Dislocation Motion

We next consider the possible forces driving the dislocation motion. In a thin-film, image stresses arising from the close proximity of the surfaces must always be considered. Dislocation boundaries, other than those that are pure tilt with the axis of rotation oriented vertically in the film, are generally unstable due to attractive interactions with the film surface(e.g., King 1997). However, such stresses do not explain the motion in the present case. The {111} twin plane lies parallel with the film surfaces, and thus the surface interaction with the horizontal dislocation segments, which are constrained to remain within the twin plane, has no component in the direction of dislocation glide.

An alternative possibility would be that the dislocations on the {111} twin are moving in response to external glide stresses, as was found by Balk et al. (2001) in their analysis of dislocation emission from a triple junctions in a thermally stressed Cu films. However, in contrast to the observations of Balk et al., where the dislocation lines were significantly curved, the dislocations in the present case remain essentially straight as they move across the twin boundary. If the motion were being driven by a glide stress on the {111} segments, the dislocations should bow outward in the direction of the applied shear since they would be pinned by the less mobile threading segments on the {112} facets, which can move only by climb.

Finally, we consider the alternative that the motion is in response to local dislocation-dislocation interactions. Because the array of edge-character SGBDs that precedes the junction is finite, it should possess a long-range strain field. In analogy with a discontinuous low angle tilt boundary composed a finite array of crystal lattice dislocations (Hirth and Lothe, 1982), the leading dislocation in the SGBD array will experience a high climb stress that increases with the number of dislocations. Thus, there is a tendency for the dislocation spacing to increase, which would reduce the misorientation and establish coincidence across the boundary. Analogous processes occur in the removal of low-angle grain boundaries through subgrain coalescence during recrystallization (Dunn and Hibbard 1955).

The important complication to this simple picture is that upon reaching the junction, the threading SGBD segments on the {112} boundary plane cannot climb further without splitting to allow one segment to move onto the diverging {112} facet and forming an additional segment of dislocation on the horizontal {111} twin plane (Fig. 6-7). Therefore, as the dislocation moves away from the facet corner, the line energy must increase with the length of the horizontal segment. This geometrical requirement will act in opposition to the repulsive interactions driving the climb.

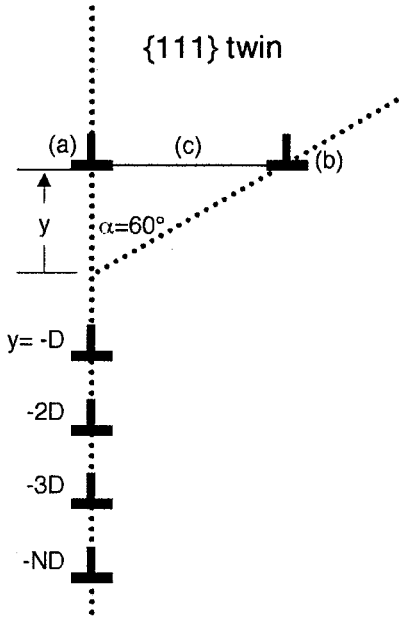

Figure 6-8: A schematic illustration of the geometry used to construct the model to determine the dislocation interaction energies.

6.5 Estimate of the Dislocation Interaction Strengths

We can estimate the relative strengths of these two competing effects by comparing the reduction in dislocation interaction energy with the corresponding increase in dislocation line energy associated with a dislocation moving out onto the {111} twin plane. We consider a simplified arrangement of dislocations that embodies the characteristics of the observed microstructure. Referring to the schematic shown in Fig. 6-8, an array of N edge dislocations, separated by a distance D, is positioned ahead of the junction ($y < 0$) on the vertical {112} facet. Beyond the junction ($y > 0$) is a single dislocation that is composed of two edge segments, labeled **a** and **b**, that lie on the two vertical {112} boundaries, and a third segment, **c**, that lies on the horizontal {111} boundary. For simplicity, we assume segment **c** is in a screw orientation and is positioned exactly midway through the film thickness.

The reduction in energy associated with the climb of segments **a** and **b** can be calculated by determining the stress-field associated with the dislocation array and then integrating the resulting Peach-Koehler force (per unit length), **F**, over the path, **r**, of the moving segments:

$$\Delta W_{int} / L = -\int \mathbf{F} \bullet d\mathbf{r} = -\int ((\mathbf{b} \bullet \boldsymbol{\sigma}) \times \boldsymbol{\xi}) \bullet d\mathbf{r} \qquad (6.1)$$

where **b** and ξ are the Burgers vector and line direction of the dislocation, L is taken as one half the film thickness, h, and σ is the tensor describing the stress field of the dislocation array. The relevant components of σ, σ_{xx} and σ_{xy}, can be computed by summing the contributions for individual dislocations within the array. Starting from the isotropic elastic solutions for an edge dislocation (e.g. Hirth and Lothe, 1982) and making the appropriate coordinate changes to treat the geometry shown in Fig. 6-8, we obtain the following:

$$\sigma_{xx} = \frac{-\mu b}{2\pi(1-\nu)} \sum_{i=1}^{N} \frac{(y+iD)(3A^2y^2 + (y+iD)^2)}{(A^2y^2 + (y+iD)^2)^2} \qquad (6.2a)$$

$$\sigma_{xy} = \frac{\mu b}{2\pi(1-\nu)} \sum_{i=1}^{N} \frac{Ay(A^2y^2 - (y+iD)^2)}{(A^2y^2 + (y+iD)^2)^2} \qquad (6.2b)$$

Here we have parameterized the expressions in terms of the y-coordinate by substituting $x=Ay$, where $A=\tan(\alpha$ ($=0$ for facet **a** and $\sqrt{3}$ for facet **b**)[†]. From these expressions, we integrate eqn. 1 over 0 to y to obtain the interaction energy for each vertical segment of length $h/2$:

$$\Delta W_{int} = \frac{-\mu b^2}{2\pi(1-\nu)} \frac{h}{2} \sum_{i=1}^{N} \left(\frac{1}{2} \ln\left(\frac{(A^2+1)y^2 + 2iDy + (iD)^2}{(iD)^2} \right) - \left(\frac{A^2y^2}{(A^2+1)y^2 + 2iDy + (iD)^2} \right) \right) \qquad (6.3)$$

In this expression, the first term in the brackets dominates such that ΔW_{int} decreases approximately logarithmically with y[††].

Additional contributions to ΔW_{int} arising from interactions between the array of threading edge dislocations and the horizontal screw segment are likely to be negligible. In fact, the total force between two infinite edge and screw dislocations with orthogonal line directions is zero provided the dislocations remain straight (*e.g.*, see section 5-4 of Hirth and

---

[†] Note that along facet **a**, σ_{xy} vanishes and σ_{xx} reduces to:

$$\sigma_{xx} = -\frac{\mu b}{2\pi(1-\nu)} \sum_{i=1}^{N} \frac{1}{y+iD}$$

[††] For $A=0$ (*i.e.*, along facet **a**) ΔW_{int} simplifies to:

$$\Delta W_{int,a} = \frac{-\mu b^2}{2\pi(1-\nu)} \frac{h}{2} \sum_{i=1}^{N} \ln\left(\frac{y+iD}{iD} \right).$$

Lothe, 1982). Furthermore, a consideration of the local interactions between orthogonal edge and screw dislocations of common Burgers vector (Hartley and Hirth 1965) also shows that there is no component of force between the dislocations in what corresponds to the *y*-direction in our geometry and no change in interaction energy associated with motion in this direction.

We next consider the increase in dislocation *line* energy that arises from the lengthening of the glissile dislocation segment as it moves out and away from the junction on the horizontal {111} twin boundary plane. The length of the dislocation, *l*, in this case is equal to $y\tan(60°) = y\sqrt{3}$. The effect of image stresses on the line energy term is treated roughly by taking the upper cut-off limit in the integration as the distance to the nearest surface (Hirth and Lothe, 1982). The line energy is then estimated from the normal expression for a screw dislocation.

$$\Delta W_{line} = l\frac{\mu b^2}{4\pi}\ln(R/r_0) = y\sqrt{3}\frac{\mu b^2}{4\pi}\ln(h/2b) \qquad (6.4)$$

Here we have taken the lower cutoff radius, r_0, to be *b*, and we have positioned the dislocation at the middle of the film, such that the upper cut-off radius, *R*, is half the film thickness (*h*/2). If the dislocation were located closer to one or the other surfaces, the line energy would be reduced correspondingly. As discussed, for instance, in section 3-2 of reference (Hirth and Lothe, 1982), it is this dependence of elastic energy on proximity of the surface that produces the image force. However, as we note at the beginning of this section, because this force is orthogonal to the twin boundary plane, it cannot drive the dislocation motion in the present geometry.

We can now compare the contributions of variation in line energy and interaction energy by summingΔW_{int} (*A*=0) , ΔW_{int} (A=$\sqrt{3}$), and ΔW_{line}. The result has been plotted in Fig. 6-9 using parameters typical of our experiment (*D*=10 nm, *h*=50 nm, μ=3.1x10^{10} Pa, and ν=0.412). When the number of dislocations in the array, *N*, is small, the line energy term immediately dominates and the total energy begins to increase once the dislocation advances only a short distance from the junction. However, as the number of dislocations in the array increases, there is a corresponding increase in the climb stresses. Therefore, for arrays containing ~10 or more dislocations, the energy continues to decrease for distances >100 nm from the junction.

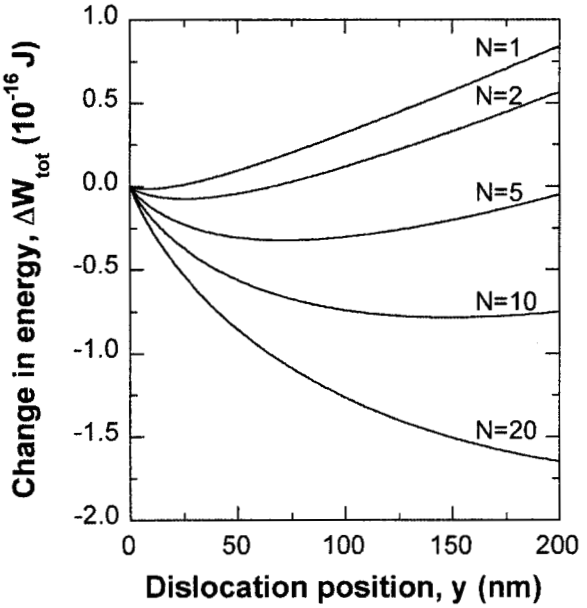

Figure 6-9: The change in dislocation interaction energy as a function of the distance of the glissile twin dislocation from the facet corner (y = 0) for different numbers of dislocations in the SGBD array (N). The glissile segment in the {111} plane will move away from the facet corner as long as the slope in relative change in energy is negative.

Since the line energy term increases linearly, whereas the interaction term decreases only logarithmically, eventually, the line energy term must always dominate. If these were the only factors involved, the dislocation must eventually stop at the point where the increase in line energy balances the reduction in interaction energy. However, this analysis shows that the repulsive interaction stresses are sufficient to drive the dislocations an appreciable distance (100-150 nm) away from the junction; a length that is comparable to the typical grain separation in these films. At these distances, the ultimate fate of the dislocation depends on the surrounding microstructure. Provided these dislocations are absorbed at microstructural sinks, such as through annihilation with other dislocations or through absorption at grain boundaries, the motion and emission of dislocations from the array can continue.

We note that as the emission process continues, a twist component must develop at the twin boundary. At least two crossed arrays of screw dislocations are required to completely relax the strain in such a boundary. For example, Forwood and Clarebrough (1986) observed an hexagonal network of 1/6 <112> dislocations composed of three *different* Burgers vectors in a near-Σ□3 {111} grain boundary with a slight twist misorientation. Therefore, the increasing amount of twist in the present boundary is compensated only

partially by an array of dislocations with a single set of parallel Burgers vectors and results in a build-up of elastic strain. If the original SGBDs were not being removed from the twin boundary, nucleation of additional dislocations is necessary to relieve this strain.

References

Balk T.J., Dehm G., and Arzt E. (2001) in *Dislocations and Deformation Mechanisms in Thin Films and Small Structures,* eds. K. Schwarz, O. Kraft, S.P. Baker, B. Freund, and R. Hull. Mat. Res. Soc. Symp. Proc., **673**, Pittsburgh, PA, p. P2.7.1.

Carter C.B. (1988), *Acta metallurgica*, **36** (10) 2753.

Carter C.B. , Medlin D.L., Angelo J.E., and Mills M.J. (1996), *Materials Science Forum* , **207-209**, 209-212.

Dahmen U. and Westmacott, K.H., 1988, *Scripta Metallurgica*, **22**, 1673.

Dash S. and Brown N. (1963), *Acta metallurgica*, **11**, 1067.

Dahmen U., Hetherington C.J. D., O'Keefe M.A., Westmacott K.H., Mills M.J., Daw M.S., and Vitek V. (1990), *Philosophical Magazine Letters*, **62** (5), 327.

Dahmen U. and Westmacott K.H. (1991), *Mat. Res. Soc. Symp. Proc.* , **229**, 167.

Daw M.S. and Baskes M.I. (1983), *Phys. Rev. Lett.* , **50**, 1285.

Dickson E. W. and Pashley D. W. (1962) *Phil Mag.*, **7**, 1315.

Dunn C.G. and Hibbard Jr. W.R. (1955), *Acta metall.*, **3**, 409.

Ernst F., Finnis M.W., Hofmann D., Muschik T., Schonberer U. and Wolf U.(1992) *Physical Review Letters*, **69** (4), 620.

Forwood C.T. and Clarebrough L.M., (1986) *Phil. Mag. Lett.*, **53**, L31.

Forwood C.T. and Clarebrough L.M. (1991), "Electron Microscopy of Interfaces in Metals and Alloys, " (Adam Hilger, Bristol) pg. 74.

Hamilton J.C. and Foiles S. M. (2002), "First-principles Calculations of Grain Boundary Theoretical Shear Strength Using Transition State Finding to Determine Generalized Gamma Surface Cross Sections", *Phys. Rev.* **B 65**(6) article number 064104.

Hamilton JC (2002), private communication.

Hartley C.S. and Hirth J.P. (1965) *Acta metall.*, **13**, 79.

Heidenreich R.D. and Shockley W. (1948) Study of slip in aluminum crystals by electron microscope and electron diffraction methods. in "Report of a Conference on the Strength of Solids," Physical Society, London 57-74.

Hetherington C.J.D., Dahmen, U., Pénisson, J.-M. , (1997) in "Atomic Resolution Microscopy of Surfaces and Interfaces," ed. D.J. Smith (MRS Proceedings, Vol. 466) 215-226.

Hetherington C.J.D. (2000) in "Problem Solving with Advanced Transmission Electron Microscopy," eds. J. Bentley *et al.,* (MRS Proceedings, Vol. 589).

Hirth J.P. and Lothe J. (1992), *Theory of Dislocations*. Krieger, New York, p. 781-783.

Hirth J.P., 1994, *J. Phys. Chem. Solids* **55** (10), 985.

Hofmann D. and Finnis M.W. (1994), *Acta metall. mater.* **42** (10), 3555-3567.

King A.H., and Smith D.A. (1980), *Acta Cryst.* A**36**, 335.

King, A.H. (1997), in *Polycrystalline Thin Films - Structure, Texture, Properties and Applications III*, eds. S.M. Yalisove, B.L. Adams, J.S. Im, Y.Zhu, and F-R. Chen. Mat. Res. Soc. Symp. Proc., **472**, Pittsburgh, PA, p. 113.

Krakow W. and Smith D.A. (1987) *Ultramicroscopy* , **22**, 47.

Lançon, F., Pénisson, J.-M., Dahmen, U. (2000), *Europhysics Letters*, **49** (5) 603.

Lançon, F. (2002), *Europhysics Letters*, **57** (1) 74.

Medlin D.L., Mills M.J., Stobbs W.M. , Daw M.S., and Cosandey F. (1993), *Mat. Res. Soc. Symp. Proc.* **295**, 91.

Medlin D.L., Campbell G.H., Carter C.B., (1998) *Acta mater.*, **46** (14), 5135-5142.

Medlin D.L., Foiles S.M., Campbell G.H., and Carter C.B., (1999)*Materials Science Forum*, **294-296**, 35-42.

Medlin D.L., Foiles S.M., and Cohen D. (2001), *Acta materialia*, **49**, 3689.

Merkle, K.L. (1990) *Colloque de Physique C1*, **51** (1), C1:251.

Merkle, K.L. (1991), *Ultramicroscopy* , **37**, 130.

Merkle, K.L. (1994), *J. Phys. Chem Solids* , 1994, **55** (10), 991.

Pashley , D.W. and Stowell, M.J. (1963) *Phil. Mag.* **8** 1605-1632.

Pénisson, J. -M., Lançon, F., and Dahmen, U. (1999) *Materials Science Forum*, **294-296**, 27.

Pond, R.C. and Vitek, V. (1977) *Proc. Royal Society London B* **357**, 453.

Pond, R.C., 1989, in "Dislocations in Solids," ed. F.R.N. Nabarro (Elsevier Science Publishers) Chapter 38, 1-66.

Pond, R.C. and Hirth, J.P. (1994), *Solid State Physics*, **47**, 287.

Ramanathan S, Clemons B.M., McIntyre P.C., Dahmen U. (2001) Philosophical Magazine A 81 (8) 2073-2094.

Rittner J.D., Seidman D.N., and Merkle, K.L. , (1996a) *Physical Review B*, **53** (8), R4241.

Rittner J.D., and Seidman D.N. (1996b) *Physical Review B*,, **54** (10), 6999.

Stowell, M.J. (1975) in "Epitaxial Growth: Part B", J.W. Matthews (ed.) (Academic Press, New York) pp. 437-492.

Sutton, A.P. and Balluffi, R.W. (1995), "Interfaces in Crystalline Materials," (Clarendon Press, Oxford) pg. 371.

Taylor, J.E. , Cahn, J.W., and Handwerker,C.A. (1992a), *Acta metall. mater.* **40**(7) 1443-1474 .

Taylor, J.E. (1992b) *Acta metall. mater.* **40** (7)1475-1485.

Tunstall, W.J., Hirsch, P.B. and Steeds, (1964) J., *Phil Mag.*, **9**, 99.

Voter, A.F. et al., (1989)in *Atomistic Simulation of Materials: Beyond Pair Potentials,* eds. V. Vitek and D. J. Srolovitz (Plenum).

Wright A.F. and Atlas S.R. (1994), *Physical Review B*, 1994, **50** (20) 15248.

Wolf, U., Ernst, F. , Muschik, T. , Finnis, M.W. and Fischmeister, H.F.(1992) *Philosophical Magazine A*, 1992, **66**, 991.

DISTRIBUTION

1	MS 1411	C.C. Battaile, 1834
1	MS 1411	E.A. Holm, 1834
1	MS 1411	S.M. Foiles, 1834
1	MS 1411	H.E. Fang, 1834
1	MS 1415	J.E. Houston, 1114
1	MS 1427	J.M. Phillips, 1100
1	MS 9011	D. Cohen, 8941
1	MS 9161	R.Q. Hwang, 8721
1	MS 9161	G. Lucadamo, 8721
1	MS 9161	D.L. Medlin, 8721
1	MS 9161	E.-P. Chen, 8726
1	MS 9161	J. Zimmerman, 8726
1	MS 9161	P.A. Klein, 8726
1	MS 9403	K.J. Gross, 8723
1	MS 9405	R.H. Stulen, 8700
1	MS 9405	D.J. Bammann, 8726
1	MS 9409	G. Kubiak, 8732
1	MS 0188	D. Chavez, LDRD Office, 4001
3	MS 9018	Central Technical Files, 8945-1
2	MS 0899	Technical Library, 9616
1	MS 0612	Review and Approval Desk, 961 For DOE/OSTI

This page intentionally left blank.